attempted to introduce the enhanced green fluorescent protein (EGFP) gene into the NOG mouse as a visible recipient marker, which if successful would make it easier to differentiate donor cells from recipient cells in studies of transplantation and regenerative medicine.

This study was performed in accordance with institutional guidelines and was approved by the Animal Experimentation Committee of the Central Institute for Experimental Animals. NOG mice expressing the EGFP gene can be obtained reliably by backcrossing with an animal in which the phenotype of the modified gene is already expressed in the donor. Therefore, we mated an inbred line of C57BL/6-*Tg(Act-EGFP)C14-Y01-FM1310sb* (C57BL/6-TgEGFP) mice [6, 8] with a NOG mice to make a NOG-EGFP (NOD.Cg-*Prkdc*^{scid} *Il2rg*^{tm1Sug} *Tg(Act-EGFP)C14-Y01-FM1310sb*/ShiJic) mice. Tail clips of the mice were obtained and digested with proteinase K using standard methods [9]. Genomic DNA was extracted using the MagExtractor System MFX-9600 Magnia R Plus (Toyobo, Osaka, Japan) according to the manufacturer's instructions. The EGFP transgene was genotyped by PCR with the forward primer GFP-F1 (5'-CTGGTCGAGCTGGACGGCGACG-3') and reverse primer GFP-R1 (5'-CACGAACTCCAGCAGGACCATG-3'). The *scid* and IL2Rg^{null} mutations were genotyped using a previously described PCR method [2, 3]. Three to six microsatellite markers were selected from each chromosome, including the X-chromosome. We selected 87 microsatellite markers to evaluate the mouse genetic backgrounds of the C57BL/6, NOG, and 129S6/SvEv strains because the Tg EGFP mice originated in C57BL/6, and the IL2Rg^{null} mutants were generated with mouse ES cells (CCE) derived from the 129S6/SvEv strain. To evaluate the genetic background in more detail, an additional 17 microsatellite markers were arranged on chromosome 9. General information about the primers, including the size of the PCR product, is listed in Table 1. First, 10–100 ng of genomic DNA was suspended in a total volume of 12.5 μl PCR buffer containing 20 mM Tris-HCl (pH 8.4), 50 mM KCl, 1.5 mM $MgCl_2$, 0.1–0.3 μM fluorescence-labeled primers, 0.2 mM dNTP, and 1.0 unit of Platinum GenoType *Tsp* DNA polymerase (Invitrogen, Carlsbad, CA, USA). Using a Bio-Rad iCycler (Bio-Rad Laboratories, Hercules, CA, USA), the thermal cycling conditions consisted of 1 cycle at 95°C for 2 min followed by: 10 cycles at 94°C for 45 s, 60°C for 1 min, and 72°C for 1 min; then, 17 cycles at 89°C for 1 min, 60°C for 1 min, and 72°C for 1 min; with a final extension of 10 min at 72°C. Following PCR, 2 μl of product, 0.6 μl of GS500-LIZ size standard (Applied Biosystems, Foster City, CA, USA), and 24.4 μl of Hi-Di formamide (Applied Biosystems) were mixed and denatured at 95°C for 2 min, cooled on ice, and then loaded directly on an ABI 3130xl Genetic Analyzer (Applied Biosystems). The electrophoresis data were processed using GeneMapper 4.0 software (Applied Biosystems). When non-labeled primer pairs were used, the PCR products were electrophoresed on 3% NuSieve 3:1 agarose (Lonza Walkersville, Inc., Walkersville, MD, USA) gel/20 mM Tris-acetate, 2.5 mM EDTA (0.5 × TAE) and then stained with ethidium bromide (0.25 μg/ml). Statistical analyses were performed with StatView 5.0 and Prism 5 software.

To introduce the EGFP transgene into NOG mice, the first generation hybrid (F_1) was obtained by mating a male C57BL/6-TgEGFP mouse as the donor with a recipient NOG female mouse. The F_1 hybrid received a uniform genome (except for the sex chromosome) from the donor and recipient, and the replacement rate (described as "% Recipient genome" in Table 2) for both the expected and observed values was 50% (Table 2). In the next stage, a randomly selected male F_1 mouse with the EGFP transgene was again mated with female NOG recipient mice to obtain the N_2 generation. Marker-assisted selection was started at the N_2 generation to select the "best" male congenic mouse. Using the 61 informative markers, the male with the closest NOG strain type was selected as the parent for the N_3 generation. Using this method, the selection of males with the closest NOG strain type was repeated four times. The observed "% Recipient genome" of the male closest to the NOG background was 81.1, 95.9, 98.4, and 99.2% in the N_2, N_3, N_4, and N_5 generations, respectively. The higher values of the observed "% Recipient genome" in generation N_3 and N_4 were statistically significant (P=0.018 and 0.067, respectively, Fisher's exact probability test). Wakeland *et al.* described the rationale of speed congenics, and stated that the advantage of screening with low-density markers (25 cM marker spacing) was realized in the N_3 and N_4 generations [12]. Com-

Table 1. MASP primer pairs and PCR product sizes in the NOG, C57BL/6, and 129S6/SvEv strains

Marker	Position (cM) [b]	NOG	C57BL/6	129S6/SvEv (CCE ES)	Dye	Marker	Position (cM) [b]	NOG	C57BL/6	129S6/SvEv (CCE ES)	Dye
D1Mit67 [a]	9	125	133	125	NED	*D9Mit182*	55	115	99	104	NL [c]
D1Mit303	34.8	112	122	112	NED	*D9Mit53*	57	198	206	198	FAM
D1Mit132 [a]	43.1	160	141	160	NED	*D9Mit184*	60	125	132	127	FAM
D1Mit91	64	146	146	138	PET	*D9Mit20*	61	95	104	114	FAM
D1Mit102 [a]	73	121	110	125	FAM	*D9Mit214*	62	135	137	108	FAM
D1Mit459 [a]	102	116	120	116	PET	*D9Mit215*	63	116	116	122	NED
D2Mit1 [a]	1	111	115	113	VIC	*D9Mit281*	68	106	111	106	FAM
D2Mit312	1	120	120	111	PET	*D9Mit120*	69	126	146	146	NL [c]
D2Mit182 [a]	38.3	149	153	149	PET	*D9Mit52* [a]	72	173	171	171	VIC
D2Mit311 [a]	83.1	110	121	115	VIC	*D10Mit2* [a*]	16	133	126	133	NED
D2Mit346 [a]	91.8	107	101	118	PET	*D10Mit31* [a]	36	146	148	151	NED
D3Mit149 [a*]	2.4	147	138	138	PET	*D10Mit266* [a]	62	82	90	84	PET
D3Mit62	4.6	117	117	110	NED	*D11Mit21* [a]	20	147	158	147	VIC
D3Mit25 [a]	29.5	127	129	123	VIC	*D11Mit67* [a]	57	133	131	122	VIC
D3Mit85 [a]	72.9	226	218	224	VIC	*D11Mit48* [a]	77	123	129	123	NED
D3Mit89 [a]	86.1	214	220	214	FAM	*D11Mit184*	78	ND	149	160	NED
D4Mit227 [a]	3.2	182	180	172	VIC	*D12Mit109* [a]	19	124	116	124	VIC
D4Mit52 [a]	54.9	110	119	112	PET	*D12Mit156* [a]	34	184	176	171	FAM
D4Mit190	79	ND	138	130	FAM	*D12Mit30*	46	103	103	113	PET
D4Mit256 [a]	82.7	128	132	128	FAM	*D12Mit133* [a]	56	96	111	111	FAM
D5Mit146 [a]	1	125	120	115	PET	*D13Mit132* [a]	4	157	150	157	NED
D5Mit1	5	135	135	129	VIC	*D13Mit13* [a]	35	145	151	145	PET
D5Mit58 [a]	41	116	114	123	NED	*D13Mit51* [a]	59	139	137	130	FAM
D5Mit367 [a]	65	96	102	92	FAM	*D14Mit1* [a]	3	101	104	98	PET
D5Mit97 [a]	74	118	124	118	NED	*D14Mit233* [a]	19.5	182	194	179	VIC
D6Mit86 [a]	0.5	121	132	121	NED	*D14Mit225* [a]	42.5	94	111	102	FAM
D6Mit284 [a]	37.5	129	138	129	FAM	*D15Mit12*	4.7	143	143	151	FAM
D6Mit304 [a]	75	105	115	107	PET	*D15Mit13* [a]	6.7	138	133	116	NED
D7Mit267 [a]	11	174	187	199	VIC	*D15Mit85*	16.4	194	194	199	FAM
D7Mit193	24.5	149	149	159	VIC	*D15Mit171* [a]	54.5	141	132	141	FAM
D7Mit350 [a]	41	138	116	122	FAM	*D15Mit42* [a]	59.2	178	182	159	VIC
D7Mit100	53.5	201	201	193	VIC	*D16Mit129* [a*]	3.4	161	180	167	PET
D7Mit189 [a]	72.4	114	129	114	PET	*D16Mit139* [a]	43.1	150	144	170	VIC
D8Mit155 [a*]	1	156	161	108	NED	*D16Mit48*	43.3	155	155	159	VIC
D8Mit217	6	169	169	179	FAM	*D16Mit106* [a]	71.5	132	142	132	PET
D8Mit191 [a]	21	122	133	122	VIC	*D17Mit163* [a]	3	126	130	124	VIC
D8Mit88 [a]	58	127	114	114	PET	*D17Mit138*	24.2	ND	138	129	FAM
D8Mit93	72	169	169	163	NED	*D17Mit53* [a]	38.5	122	128	122	VIC
D9Mit250	5	123	123	132	VIC	*D17Mit93* [a]	44.5	141	154	141	NED
D9Mit83 [a]	6	129	134	134	PET	*D18Mit19*	2	150	150	133	FAM
D9Mit97 [a]	29	162	151	159	VIC	*D18Mit12* [a]	17	122	110	110	FAM
D9Mit102	31	144	140	144	FAM	*D18Mit91* [a]	29	135	137	137	PET
D9Mit207	33	160	148	155	NL [c]	*D18Mit40*	37	135	137	137	FAM
D9Mit105	35	116	145	145	NL [c]	*D18Mit187* [a]	47	106	110	110	FAM
D9Mit259	38	122	112	115	NL [c]	*D18Mit25*	57	117	117	109	NED
D9Mit107	40	119	120	104	FAM	*D19Mit78* [a]	5	130	126	128	FAM
D9Mit8	42	185	178	169	VIC	*D19Mit14* [a]	15	150	153	146	PET
D9Mit124	42	128	124	124	FAM	*D19Mit103* [a]	52	117	115	123	NED
D9Mit236	43	125	143	125	NL [c]	*DXMit55* [a]	1.4	121	129	127	NED
D9Mit11	48	112	74	100	NL [c]	*DXMit25* [a]	27.8	158	168	158	VIC
D9Mit275	50	115	110	110	FAM	*DXMit130*	55	161	161	136	VIC
D9Mit35	52	112	124	124	NL [c]	*DXMit121* [a]	67	130	147	147	VIC

[a]: Informative microsatellite markers for distinguishing between the NOG and C57BL/6 strains; [b]: according to the Mouse Genome Database (MGD; http://www.informatics.jax.org); *: Primers were changed from the original sequence on the NCBI UniSTS database to redesigned sequences in order to change the size of the PCR product as follows; *D3Mit149*: F 5'-TTCCATACAAACAAAAGCAACG-3', R 5'-CTATATAGCTGTAAATGTAAAGTGTATGTC-3', *D8Mit155*: F 5'-TTGGACAGGGAAAATTCTGC-3', R 5'-GAAAATGTGACACCATTTGAGGAC-3', *D10Mit2*: F 5'-GTTCATTTGAGGCACAAGCA-3', R 5'-TTTGAGCTGCTCACAACCC-3', and *D16Mit129*: F 5'-ATGAGCAGTCTGCAGACCTT-3', R 5'-GAGACTGAGAAAGGGGATGC-3'; [c]: non-labeled primer pairs; ND: not detected.

Table 2. Comparison of the methods used to generate NOG-EGFP mice

Generation number[a] (Number examined[b])	% Recipient genome (R/total)[c]			
	Expected	Observed		
		MAX	MIN	AVG ± SD
P	0	–	–	–
F_1	50 (61/122)	50 (61/122)	–	–
N_2 (13)	75 (91.5/122)	81.1 (99/122)	66.4 (81/122)	73.1 ± 4.1
N_3 (15)	87.5 (106.8/122)	95.9 (117/122) *	88.5 (108/122)	91.3 ± 2.4
N_4 (31)	93.8 (114.4/122)	98.4 (120/122) **	95.9 (117/122)	96.9 ± 0.8
N_5 (4)	96.9 (118.2/122)	99.2 (121/122)	98.4 (120/122)	98.8 ± 0.5

[a]The generation count begins at strain P (parental) defined as 100% original background, 0% recipient background. The F_1 generation contains the offspring from the intercross between P (100% original) × pure recipient NOG strains (100% recipient). F_1 animals have 50% of the recipient genome. [b]The numbers of transgenic male mice whose genetic backgrounds were examined. [c]R: the number of homozygotes for the allele of the recipient strain; total: total number of alleles. *P=0.015 and **P=0.095 (Fisher's exact probability test).

puter simulations of MASP-based congenic strain construction strategies using high-density (10 cM apart) and low-density (25 cM apart) marker spacing, and screening a mean of 40 and 16 progeny per generation revealed that screening 16 progeny per generation with a low-density marker was the most cost-effective strategy. Our MASP strategy is similar to the computer-simulated most cost-effective strategy because 61 informative microsatellite markers were arranged throughout the mouse genome spaced at an average distance of 26.5 cM (low density), and we screened 13, 15, and 31 progeny at N_2, N_3, and N_4, respectively. However, our MASP strategy included some gaps of over 30 cM, with a largest gap of 51.7 cM. One major problem is that a larger gap might not be able to detect a double crossing-over occurring in meiosis. Hameister *et al.* examined the frequency of double crossing-over in a 55.4-cM region between chromosome 15A2 and 15F2-3 in 151 mice and found only one animal with a double crossing-over [2]. In reality, double crossing-over does not occur at a high frequency, even in a larger gap extending over 50 cM. Therefore, detecting double crossing-over using adjacent markers might be possible. Another problem is the inability to detect a small segment of the donor genome. Because screening all gaps over 30 cM is unrealistic, we screened one large gap (43 cM) extending between *D9Mit97* and *D9Mit52* in more detail. We used extremely high-density markers (2.4 cM marker spacing) consisting of 17 informative markers in 12 and 14 progeny at N_2 and N_3, respectively. No animal with a double crossing-over was found in 12 animals in the N_2 generation, while a small contaminating segment of the donor genome was detected between markers *D9Mit207* and *D9Mit107* in progeny #E109 of the N_3 generation (Fig. 1). Considering an undetected contaminating donor genome, Wakeland *et al.* recommended performing one or two additional backcrosses when all of the markers become recipient-derived. This additional backcross reduces the level of undetected contamination in these strains to the equivalent of that at N_{10} or N_{11} using the traditional protocol [12]. When transferring a transgene or modified gene into the NOG or C57BL/6 strain from C57BL/6 or NOG and 129S6/SvEv backgrounds, our selected 61 markers serve as genetic quality standards for generating a congenic strain using MASP. The final backcross could be completed because the NOG-EGFP mouse (N_5) met the genetic quality standards after backcrossing four times. However, we persisted with backcrossing during the production of congenic progeny derived from the N_5 generation for xenotransplantation studies. This additional backcross might confer some benefit through the further elimination of residual donor genomes.

To examine the phenotype of the NOG-EGFP mice, the male mouse closest to the NOG strain with EGFP transgene in the N_5 generation was mated with female NOG mice to obtain many NOG-EGFP mice (N_6) for xenotransplantation studies. NOD/Shi-*scid* mice (male, 10 weeks old), NOG mice (female, 7 weeks old), and NOG-EGFP mice (female, 12 weeks old) were irradiated with 2.4 Gy of X-rays 24 h before transplanting 5

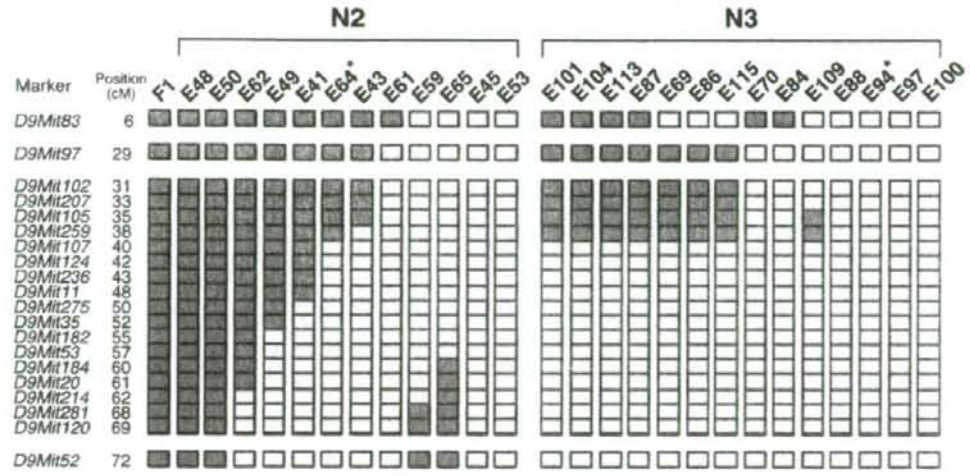

Fig. 1. Detailed screening between *D9Mit97* and *D9Mit52* using extremely high-density markers (2.4 cM marker spacing). The screening is depicted schematically using genotyping data in which each box indicates one informative microsatellite marker primer pair. The yellow boxes represent those PCR products that are identified as NOG homozygotes based on size. The red boxes represent C57BL/6 and NOG heterozygotes. The asterisks indicate the "best" males that were selected as the parents of the next backcross generation.

$\times 10^4$ human CD34$^+$ cells (Lonza Walkersville, Inc.). The engraftment of donor cells was monitored every 4 weeks by detecting the human cells expressing the leukocyte common Ag CD45 (Immunotech, Marseille, France) using a MoFlo flow cytometer (Dako, Glostrup, Denmark) and Summit software. Representative flow cytometric analysis of peripheral blood of mice that underwent transplantation (after 12 weeks) is shown in Fig. 2a. When using NOG-EGFP mice as recipients, we could easily differentiate donor human cells from recipient mouse cells with the fluorescent signals of the EGFP, although the cells were not stained with any cell surface marker for the mouse species. Twelve weeks after transplantation, significantly more growth of human cells was observed in both NOG mice and NOG-EGFP mice compared to NOD/Shi-*scid* mice ($*P<0.01$; $**P<0.001$; Fig. 2b), but there was no significant difference between NOG mice and NOG-EGFP mice. These results suggest that the NOG-EGFP mice, which were generated by the congenic method with MASP, acquired the immunological properties of the NOG strain.

In this experiment, we did not use X-chromosome-derived microsatellite markers as informative markers to select a parent for the next generation because the X-chromosome is always derived from the recipient NOG strain in male transgenic mice. However, we checked the X-chromosome with informative markers to distinguish between the NOG and 129S6/SvEv strains (the source of the CCE ES cells) because of the confirmation of an X-chromosome linked IL2Rg^{null} mutation (Chr X, 38 cM) derived from the recipient genome. However, the nearest marker located at 32.1 cM was not informative, and the other three markers on the X-chromosome were shown to be homozygous for recipient-derived alleles.

Nakanishi *et al.* analyzed transgene integration sites in more than 100 EGFP transgenic mouse lines rigorously using fluorescent *in situ* hybridization and determined that the EGFP transgene is located on the D1 region of chromosome 14 in the 131 line (C57BL/6-*Tg (Act-EGFP) C14-Y01-FM1310sb*) [6]. The microsatellite markers that did not become NOG markers in the N_4 generation were the markers *D14Mit233* and *D14Mit225*, both of which are on chromosome 14. Fortunately, we could change the genetic background around the *D14Mit225* region from C57BL/6 to the NOG strain in the N_5 generation, but the genetic background around the *D14Mit233* region remained C57BL/6. *D14Mit233*

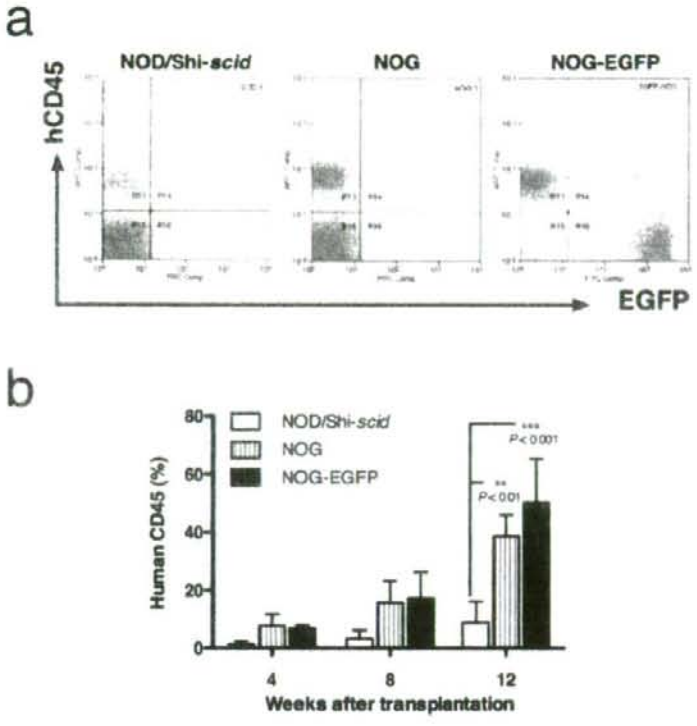

Fig. 2. High engraftment efficiency of human cells in NOG-EGFP mice. (a) Representative flow cytometric data for peripheral blood obtained from NOG-EGFP mice that underwent human cord blood CD34$^+$ cell transplantation (12 weeks after transplantation). (b) Comparison of the engraftment levels of human cells in NOD/Shi-*scid*, NOG, and NOG-EGFP mice. At the indicated times following transplantation of 5×10^4 CD34$^+$ cells, human CD45$^+$ cells in mouse peripheral blood were assayed by flow cytometry (n=3 each). $^{**}P<0.01$, $^{***}P<0.001$.

and *D14Mit225* are located in the B and D1–D3 regions, respectively. These markers are located extremely close to the site of EGFP transgene integration in the C5BL/6-TgEGFP line 131. The *D14Mit233* marker seemed to be closer to the integrated transgene than the *D14Mit225* marker because six recombinants at the *D14Mit225* locus were observed in the 63 male Tg EGFP mice, while no recombinant was observed for the *D14Mit233* marker. The distance from the *D14Mit225* marker to the integrated EGFP transgene can be calculated as roughly 9.5 cM based on the recombination frequency [10]. Based on statistical modeling, the traditional 12 backcross generation (N_{12}) protocol will produce a congenic strain in which more than 99% of the genome is unlinked to the target gene carried in a donor-derived genome segment with an average length of about 20 cM [1]. Therefore, the *D14Mit233* marker genetically linked to the transgene integration site is physically close enough to the transgene that it will not segregate independently during meiosis.

Acknowledgment(s)

We thank Noriko Omi and Chika Kito of CIEA for their technical assistance and Dr. Masaru Okabe (Osaka University) for providing the green mice.

References

1. Flaherty, L. 1981. pp. 215–221. *In*: The Mouse in Biomedical Research: History, Genetics, and Wild Mice, Vol. 1, (Foster, H.L., Small, J.D., and Fox, J.G., eds.). Academic Press, New York.
2. Hameister, H., Schulz, W.A., Meyer, J., Thoma, S., Adolph, S., Gua, A., and von Deimling, O. 1992. *Genomics* 14: 417–422.
3. Ito, M., Hiramatsu, H., Kobayashi, K., Suzue, K., Kawahata, M., Hioki, K., Ueyama, Y., Koyanagi, Y., Sugamura, K., Tsuji, K., Heike, T., and Nakahata, T. 2002. *Blood* 100: 3175–3182.
4. Koyanagi, Y., Tanaka, Y., Kira, J., Ito, M., Hioki, K., Misawa, N., Kawano, Y., Yamasaki, K., Tanaka, R., Suzuki, Y., Ueyama, Y., Terada, E., Tanaka, T., Miyasaka, M., Kobayashi, T., Kumazawa, Y., and Yamamoto, N. 1997. *J. Virol.* 71: 2417–2424.
5. Maruyama, C., Suemizu, H., Tamamushi, S., Kimoto, S., Tamaoki, N., and Ohnishi, Y. 2002. *Exp. Anim.* 51: 391–393.
6. Nakanishi, T., Kuroiwa, A., Yamada, S., Isotani, A., Yamashita, A., Tairaka, A., Hayashi, T., Takagi, T., Ikawa, M., Matsuda, Y., and Okabe, M. 2002. *Genomics* 80: 564–574.
7. Ohbo, K., Suda, T., Hashiyama, M., Mantani, A., Ikebe, M., Miyakawa, K., Moriyama, M., Nakamura, M., Katsuki, M., Takahashi, K., Yamamura, K., and Sugamura, K. 1996. *Blood* 87: 956–967.
8. Okabe, M., Ikawa, M., Kominami, K., Nakanishi, T., and Nishimune, Y. 1997. *FEBS Lett.* 407: 313–319.
9. Sambrook, J. and Russell, D.W. 2001. Molecular Cloning. Third Edition: A Laboratory Manual. Cold Spring Harbor Laboratory Press, New York.
10. Sturtevant, A.H. 1913. *J. Exp. Zool.* 14: 43–59.
11. Teppner, I., Aigner, B., Schreiner, E., Müller, M., and Windisch, M. 2004. *Lab. Anim.* 38: 406–412.
12. Wakeland, E., Morel, L., Achey, K., Yui, M., and Longmate, J. 1997. *Immunol. Today* 18: 472–477.
13. Wong, G.T. 2002. *Neuropeptides* 36: 230–236.

Biochemical and Biophysical Research Communications 377 (2008) 248–252

Contents lists available at ScienceDirect

Biochemical and Biophysical Research Communications

journal homepage: www.elsevier.com/locate/ybbrc

Establishment of a humanized model of liver using NOD/Shi-*scid* IL2Rg^{null} mice

Hiroshi Suemizu [a,*,1], Masami Hasegawa [a,d,1], Kenji Kawai [b], Kenji Taniguchi [a,d], Makoto Monnai [a,e], Masatoshi Wakui [b,f], Makoto Suematsu [f], Mamoru Ito [c], Gary Peltz [g,2], Masato Nakamura [b,h]

[a] Biomedical Research Department, Central Institute for Experimental Animals, 1430 Nogawa, Miyamae, Kawasaki, Kanagawa 216-0001, Japan
[b] Pathology Research Department, Central Institute for Experimental Animals, 1430 Nogawa, Miyamae, Kawasaki, Kanagawa 216-0001, Japan
[c] Laboratory Animals Research Department, Central Institute for Experimental Animals, 1430 Nogawa, Miyamae, Kawasaki, Kanagawa 216-0001, Japan
[d] Pharmaceutical Research Department II, Chugai Pharmaceutical Co., Ltd., 200 Kajiwara, Kamakura, Kanagawa 247-8530, Japan
[e] Chugai Research Institute for Medical Science, Inc., 200 Kajiwara, Kamakura, Kanagawa 247-8530, Japan
[f] Department of Biochemistry and Integrative Medical Biology, Keio University School of Medicine, 35 Shinanomachi, Shinjuku, Tokyo 160-8582, Japan
[g] Department of Genetics and Genomics, Roche Palo Alto, 3431 Hillview Avenue, Palo Alto, CA 94304-1397, USA
[h] Department of Pathology, Tokai University School of Medicine, 143 Shimokasuya, Isehara, Kanagawa 259-1193, Japan

ARTICLE INFO

Article history:
Received 10 September 2008
Available online 7 October 2008

Keywords:
Humanized mouse
Liver repopulation
NOD/Shi-*scid* IL2Rg^{null} (NOG) mouse
Urokinase-type plasminogen activator

ABSTRACT

Severely immunodeficient NOD/Shi-*scid* IL2Rg^{null} (NOG) mice are used as recipients for human tissue transplantation, which produces chimeric mice with various types of human tissue. NOG mice expressing transgenic urokinase-type plasminogen activator in the liver (uPA-NOG) were produced. Human hepatocytes injected into uPA-NOG mice repopulated the recipient livers with human cells. The uPA-NOG model has several advantages over previously produced chimeric mouse models of human liver: (1) the severely immunodeficient NOG background enables higher xenogeneic cell engraftment; (2) the absence of neonatal lethality enables mating of homozygotes, which increased the efficacy of homozygote production; and (3) donor xenogeneic human hepatocytes could be readily transplanted into young uPA-NOG mice, which provide easier surgical manipulation and improved recipient survival.

The metabolism of xenobiotic compounds, including medicinal drugs, predominantly occurs in the liver. Due to the significant inter-species differences in many liver enzymes that mediate drug metabolism, the metabolism of candidate pharmaceuticals is usually initially evaluated *in vitro* using human cells or cell extracts [1,2] or *in vivo* in rodent models. Although *in vivo* pharmacokinetic studies are routinely performed in experimental animal models, significant inter-species differences in drug metabolism limit their ability to predict human drug metabolism. There are many examples where the findings from rodent models do not extrapolate to man. *In vitro* studies using transformed human hepatic cells, human hepatocytes or human hepatocyte extracts have also been used to predict human drug metabolism. Although they utilize human cells, *in vitro* systems have a very limited ability to predict human drug metabolism *in vivo*. Drug-induced alterations of the level of expression of drug metabolizing enzymes, which is a common problem in clinical medicine, does not occur in the *in vitro* extracts. In addition, the pattern of expression of drug metabolizing enzymes is altered within a very short time period after hepatocytes are cultured *in vitro* (reviewed in [2]). Human drug metabolizing enzymes have been expressed as transgenes in mice. For example, a mouse expressing a human CYP2D6 transgene in liver had a human-specific profile of metabolism of a test substrate [3]. However, transgenic expression of one or a few human enzymes in mouse liver does not represent the biotransformation capabilities of human liver.

To overcome the limitations associated with currently used *in vitro* and *in vivo* experimental methods for studying drug metabolism and toxicity, investigators have utilized several different methods for producing chimeric mice with artificial human livers. Historically, chimeric mice have been generated by introducing human tissues or cells into immune deficient SCID mice, which have an inactivating mutation in the catalytic subunit of the DNA-dependent protein kinase (Prkdc^{scid}, known as the *scid* mutation). Ralph Brinster and colleagues demonstrated that transgenic expression of urokinase-type plasminogen activator (AL-uPA) within mouse liver directed by an albumin promoter caused progressive damage to liver parenchymal cells [4,5]. The mice usually died within weeks due to progressive liver failure. Although the mechanism of hepatic cell destruction has not fully characterized in detail; uPA regulates the activation of plasminogen, which controls the activation of matrix metalloproteinases that are critical for liver cell growth (reviewed in [6]). In addition, the livers in surviving mice are replaced at 8–12 weeks of age by nodular growths that have deleted the transgene. In an elegant series of experi-

* Corresponding author. Fax: +81 44 754 4465/4454.
E-mail address: suemizu@ciea.or.jp (H. Suemizu).
[1] These authors contributed equally to this work.
[2] Present address: Department of Anesthesia, Stanford University, Stanford, CA 94305-5796, USA.

0006-291X/$ - see front matter © 2008 Elsevier Inc. All rights reserved.
doi:10.1016/j.bbrc.2008.09.124

ments, investigators showed that the AL-uPA mice could be rescued from liver failure by transplant of congenic or xenogenic hepatocytes [7–10]. Other investigators subsequently demonstrated that immunocompromised (recombinant activation gene-2; RAG-2 deficient or SCID mutation) mice expressing this transgene could be partially repopulated (~15%) with human hepatocytes [9,10].

Recently, we developed NOD/Shi-*scid* IL2Rg^{null} (NOG) mice by crossing IL-2 receptor gamma chain-deficient (IL2Rg^{null}) mice [11] with NOD/Shi-*scid* mice [12]. NOG mice lack T and B lymphocytes and natural killer (NK) cells, and they have impaired dendritic cell function [13–15]. Because of their severe immunodeficient state, NOG mice have been used as an *in vivo* model to study human hematopoietic stem cell [13,14] and endometrial tissue [16,17] engraftment. Here, we used NOG mice to develop an uPA/NOG-transgenic model that allows the engraftment of human hepatocytes into a damaged liver. This model could provide a useful tool for characterization of hepatic drug metabolism *in vivo* within a humanized liver.

Materials and methods

Transgenic mice. The mouse albumin promoter-driven urokinase-type plasminogen activator (*Plau*, known as uPA) gene expression unit (GenBank Accession No. AB453180) was constructed as follows. The 2345-bp *Not*I–*Bam*HI fragment of the mouse albumin enhancer/promoter from plasmid p2335A-1 [18], the 304-bp *Hin*dIII–*Nhe*I fragment of the chimeric intron from pCI plasmid (Promega Corp., WI, USA), the 1367-bp *Nhe*I–*Sal*I fragment of the PCR-amplified mouse uPA cDNA (MuPA-Nhe1-F, 5′-GCTA GCGGCACTACCATGAAAGTC-3′; MuPA-Sal1-R, 5′-AATTAAGTCGACA ACAAGTGACCC-3′), and the 624-bp *Sma*I–*Eco*RI fragment of the PCR-amplified human growth hormone (*GH1*) 3′-flanking region (hGHF, 5′-GCTCTACTGCTTCAGGAAGGACAT-3′; hGHR, 5′-GAATTCA ACAGGCATCTACTGA-3′) were cloned into the pBlueScript II vector (Promega) with appropriate polylinkers (5′-GATCCAAGCTTATGC AGTCGACCCGGGCATGCGAATTCTCGA-3′). A vector-free, 4.6-kb uPA expression fragment was prepared by *Not*I and *Kpn*I digestion and microinjected into fertilized NOD/Shi strain mouse eggs using standard methods. Transgenic founders were mated with NOD-Cg-*Prkdc*^{scid} *Il2rg*^{tm1Sug}/ShiJic (NOG) mice to confer the *scid* and IL2Rg^{null} mutations. The *scid* and IL2Rg^{null} mutations were genotyped by PCR as described previously [13,19]. The mice were assigned the following genetic designation: NOG-*Tg(Alb-Plau)11-4*/ShiJic [formally, NOD-Cg-*Prkdc*^{scid} *Il2rg*^{tm1Sug} *Tg(Alb-Plau)11-4*/ShiJic; abridged name: uPA-NOG]. The present study was performed in accordance with institutional guidelines and was approved by the Animal Experimentation Committee of the Central Institute for Experimental Animals.

Detection of uPA transcripts by RT-PCR. Total cellular RNA samples from the liver, kidney, and spleen were obtained from 29-week-old uPA-NOG mice using the RNeasy Mini kit (QIAGEN, Tokyo, Japan). Reverse transcription-polymerase chain reaction (RT-PCR) was performed using the High Capacity cDNA Reverse Transcription kit (Applera Corporation, CA, USA). The spMuPAF forward primer (5′-GAGGCACTGGGCAGGTGTCC-3′) and MuPAR reverse primer (5′-AGGGCCGACCTTTGGTATCAGTG-3′) were used to detect the spliced form of the external mouse uPA transcript (365-bp band). The 479-bp glyceraldehyde-3-phosphate dehydrogenase (*Gapdh*) fragment was amplified using the G3PDHF forward primer (5′-TCACCATCTTCCAGGAGCGAGA-3′) and the G3PDHR reverse primer (5′-GAAGGCCATGCCAGTGAGCTT-3′) and used as an internal control.

Spontaneous liver damage. The degree of liver damage was examined by determining the serum levels of alanine aminotransferase (ALT). Clinical biochemical analyses of serum samples were carried out with the Fuji DRI-CHEM 7000 (FUJIFILM Corporation, Tokyo, Japan).

Southern blot analyses. Genomic DNA samples from liver and kidney were obtained from 8-week-old uPA-NOG mice and non-transgenic mice by overnight incubation with proteinase K and subsequent extraction with phenol: chloroform: ethanol according to the standard protocol. *Xba*I, *Xho*I, *Bgl*II, and *Bam*HI restriction enzyme-digested genomic DNA was electrophoresed on a 0.6% agarose gel and transferred to a positively charged nylon membrane (F. Hoffmann-La Roche Ltd., Basel, Switzerland). Hybridization was carried out with a DIG-labeled probe that was prepared using the PCR DIG Probe Synthesis Kit (F. Hoffmann-La Roche Ltd.) using forward (5′-GTTCTCCAGCTTGGGATCGACCTG-3′) and reverse (5′-TTGATAGGAAAGGTGATCTGTGTGCAG-3′) primers according to the manufacturer's instructions.

Transplantation of human hepatocytes. Commercially available cryopreserved hepatocytes (Lonza Walkersville Inc., MD, USA) were used as donor cells. Young (6-week-old) uPA-NOG hemizygotes and homozygotes were used as recipients. Cell number and viability were determined by trypan blue exclusion in a hemocytometer. One million viable hepatocytes in 40 μl of Hank's Balanced Salt Solution (HBSS) were injected intrasplenically via a Hamilton syringe with a 26 G needle.

Human albumin measurements. Small volumes of blood were collected biweekly from the retro-orbital venousplexus with a plastic capillary. After a 500- to 30,000-fold dilution with Tris-buffered saline that contained 1% bovine serum albumin and 0.05% Tween-20, human albumin concentrations were measured with the Human Albumin ELISA Quantitation Kit (Bethyl Laboratories Inc., TX, USA) according to the manufacturer's protocol.

Immunoblotting. Diluted serum samples (2000× dilution) were solubilized in SDS sample buffer with 5% β-mercapthoethanol. Proteins were subjected to SDS–PAGE and transferred to Hybond-ECL membranes (GE Healthcare Bio-Sciences Corp., NJ, USA). The membranes were incubated for 90 min with biotinylated polyclonal goat anti-mouse albumin antibodies (A90-234A; Bethyl Laboratories) and biotinylated polyclonal goat anti-human albumin antibodies (A80-229A; Bethyl Laboratories), washed, and incubated with a streptavidin–horseradish peroxidase conjugate (GE Healthcare Bio-Sciences) for 60 min. The biotinylated antibodies were prepared using the FluoReporter Mini-Biotin-XX Protein Labeling Kit (Invitrogen Corp., CA, USA). The immunoblots were developed using the ECL Western Detection System and Hyperfilm ECL (GE Healthcare Bio-Sciences).

Histology and immunohistochemistry. The tissues were fixed with 4% (v/v) phosphate-buffered formalin, and paraffin-embedded sections were stained with hematoxylin and eosin (H&E). Polyclonal goat anti-human albumin antibodies (Bethyl Laboratories) were used as the primary antibodies. The antibodies were visualized using amino acid polymer/peroxidase complex-labeled anti-goat Ig antibody (Histofine Simple Stain Mouse MAX PO (G); Nichirei Bioscience Inc., Tokyo, Japan) and diamino-benzidine (DAB; Dojindo Laboratories, Kumamoto, Japan) substrate [0.2 mg/ml 3,3′-diaminobenzidinetetrahydrochloride, 0.05 M Tris–HCl (pH 7.6), and 0.005% H_2O_2]. Sections were counter-stained with hematoxylin.

Statistical analyses. Statistical analyses were performed with StatView ver. 5.0 (SAS Institute, Tokyo, Japan) and the Prism 5 software (GraphPad Software, CA, USA).

Results and discussion

Previously prepared AL-uPA transgenic mice [*Tg(Alb-1,Plau)-Bri144* lines 1353–8 and lines 1944–6] possess five or 10 copies,

respectively, of the transgene joined head-to-tail in a tandem array [20]. In both lineages, half of the transgenic offspring bled extensively and died as neonates. Neonatal lethality was correlated with the level of expression of the uPA transgene, which is determined, at least in part, by the copy number. Therefore, we predicted that mice with fewer copies of the uPA transgene would have less liver damage, which would eliminate the uPA-mediated neonatal lethality. We produced uPA-transgenic mice in severely immunodeficient NOG mice [NOG-*Tg(Alb-Plau)11-4*/ShiJic, referred to as uPA-NOG] with the uPA gene expression unit (Fig. 1A). RT-PCR analysis

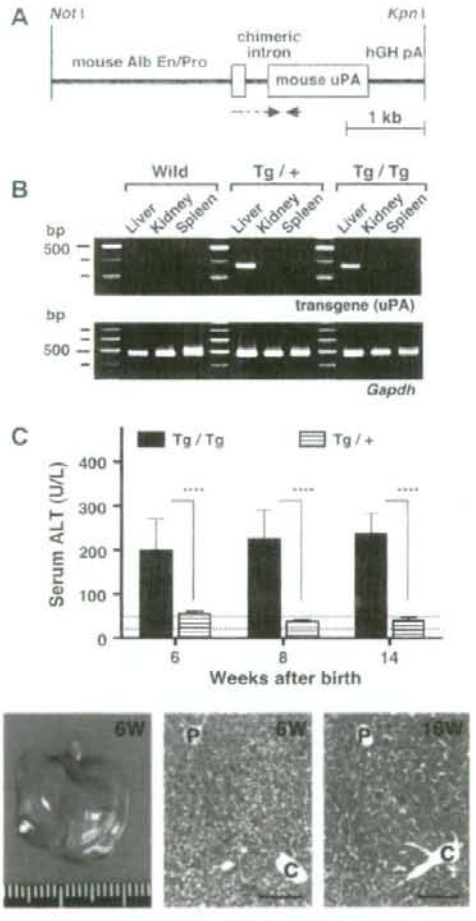

Fig. 1. Establishment of the uPA-NOG mouse as a model of spontaneous hepatic injury. (A) The uPA expression unit contains the mouse albumin enhancer/promoter (Alb En/Pro), the chimeric intron, mouse uPA cDNA, and the 3′-UTR of the human growth hormone gene with polyadenylation (pA) signal. Arrowheads depict the positions and directions of the RT-PCR primers. (B) RT-PCR analyses of uPA transgene expression. Wild, non-transgenic NOG; Tg/+, hemizygous; and Tg/Tg, homozygous uPA-NOG mice. *Gapdh* was used as an internal control. (C) ALT activities in uPA-NOG mice. All the values for the homozygous uPA-NOG (Tg/Tg) are significantly higher than those for the hemizygote (Tg/+) ($P < 0.0001$, unpaired *t*-test). Dashed lines indicate the two standard deviation ranges for the values for the non-transgenic NOG mice ($n = 7$). Each of the points for the hemizygous and homozygous uPA-NOG mice represent the mean ± SD of four to seven samples. (D) Gross appearance and histopathology of a homozygous uPA-NOG mouse liver. Scale bar, 100 μm; P, portal tract; C, central vein.

of uPA transgene expression indicated that the chimeric introns were appropriately spliced to produce the uPA expression unit. Although the transgene was expressed in the livers of hemizygous (Tg/+) and homozygous (Tg/Tg) uPA-NOG mice; it was not expressed in the kidneys, spleens or any other tissues obtained from non-transgenic NOG mice (Fig. 1B). uPA-NOG hemizygotes were indistinguishable from non-transgenic littermates; they have never exhibited spontaneous intestinal or intra-abdominal bleeding that was typically seen in previously produced AL-uPA transgenic mice [21]. The level of expression of the transgene in hemizygous uPA-NOG mice was below that required to cause liver disease. The serum ALT activity in the hemizygote, an indicator of hepatocyte damage, did not increase in mice at any age and was identical to that of a non-transgenic NOG mouse (Fig. 1C).

Since transgene zygosity affects the phenotype of transgenic mice via a gene dosage effect; we produced a homozygous line of uPA-NOG mice that carries two copies of the transgene array that stably reinforces transgene expression. To do this, female and male homozygotes were bred to produce homozygous uPA-NOG mice, which no longer needed progeny testing or genotyping for zygosity. At birth, the homozygotes, whose zygosity was confirmed by progeny testing, were slightly smaller than their hemizygous littermates. Quantitative RT-PCR revealed that transgene expression in the livers of homozygous uPA-NOG mice was 2.4- to 3.6-fold higher than hemizygotes (data not shown). However, perinatal hemorrhaging, embryonic lethality or neonatal lethality did not occur in homozygous uPA-NOG mice. The serum ALT level (75.0 ± 9.1, $n = 4$) in the homozygote at 4 weeks of age was slightly above that of the hemizygote, but this trend did not reach statistical significance (data not shown). However, the ALT levels began to increase by 6 weeks of age in the uPA-NOG homozygotes, and remained elevated through 14 weeks of age (Fig. 1C). The livers of 6-week-old uPA-NOG homozygotes had evidence of modest hepatic injury. The hepatocytes focally showed degeneration foci and a few eosinophilic bodies predominantly around the central veins (Fig. 1D, center). The livers of 16-week-old uPA-homozygous mice revealed megalocytosis with increased eosinophilic bodies (Fig. 1D, right).

The phenotype and liver histology of uPA-NOG mice was significantly different from that of previously produced AL-uPA transgenic mice. uPA-NOG mice did not develop the severe edema that was observed AL-uPA homozygote mice at 3–6 weeks of age [4]. The color of the liver parenchyma was also significantly different. The livers of 3- to 5-week-old AL-uPA-transgenic homozygotes were smooth and pale to nearly white in color (known as "white liver"), and the livers of the hemizygotes were also profoundly abnormal in appearance, with multiple reddish nodules in addition to the white parenchyma [4]. However, the liver of 6-week-old homozygous uPA-NOG mouse did not show any "white liver" changes, regardless of uPA transgene zygosity (Fig. 1D, left). AL-uPA transgenic mice have an age-dependent decrease in uPA expression that is caused by deletion of the integrated transgene [4]. However, Southern blot analysis indicated that the transgene array was stably integrated at a single locus in the uPA-NOG homozygote (Fig 2A). The fact that there were no differences in hybridization banding patterns in the liver and kidney DNA samples in 8-week-old uPA-NOG mice indicate that there is a relatively low frequency of physical loss of the transgene from uPA-NOG mice. Furthermore, stable level of expression of the uPA transgene (Fig. 1B) and the persistence of high levels of the hepatic injury marker (ALT) also indicate the transgene is stably expressed (data not shown). Further analysis of the banding pattern after *Xho*I digestion indicate that uPA-NOG mice have at least three copies of the 4.6-kb monomeric transgene. The low copy number of the integrated transgene in uPA-NOG mice may prevent neonatal lethality. The architecture of the integrated transgene in uPA-NOG mice was further analyzed by southern blot analyses with additional restric-

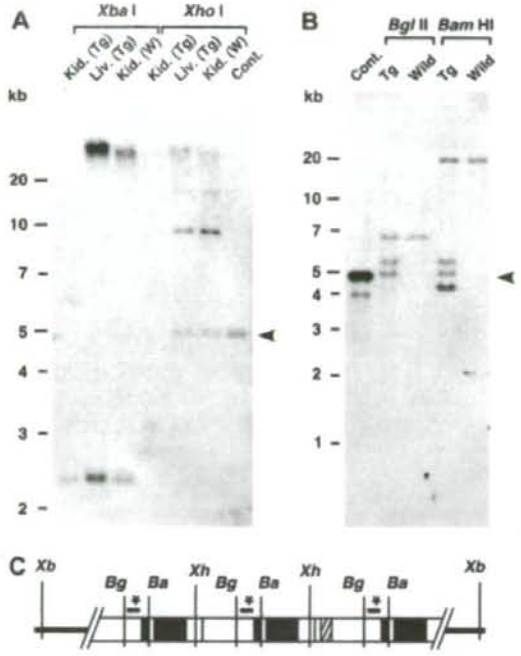

Fig. 2. Molecular analyses of the integrated transgene in uPA-NOG mice. (A) DNA samples from non-transgenic NOG mouse kidney (Kid.; W) and uPA-NOG hemizygote kidney (Kid.; Tg) and liver (Liv.; Tg) were digested with XbaI and XhoI for Southern blot analysis. (B) DNA samples from non-transgenic NOG mouse kidney (Wild) and uPA-NOG hemizygote kidney (Tg) was digested with BglII and BamHI. The uPA expression unit (4.6-kb fragment) was used as a positive control (arrowhead). (C) Restriction map and structure of the transgene in uPA-NOG mice. Solid boxes indicate transcribed segments. Asterisks indicate the positions recognized by DIG-labeled probes. The shaded box indicates the rearranged region. Restriction enzymes: Xb, XbaI; Xh, XhoI; Bg, BglII; Ba, BamHI.

tion enzymes (Fig 2B) to produce the restriction map of the integrated transgene array (Fig. 2C). This array consists of at least three copies of the uPA gene expression unit joined head-to-tail in a tandem array. One of the uPA gene expression units that located at downstream position had a small rearrangement (Fig. 2C). However, the rearrangement was likely not an acquired characteristic, because the rearrangement was observed in the founder mice from this line (data not shown).

To determine whether uPA-NOG mice could support repopulation by transplanted hepatocytes, commercially available cryopreserved human hepatocytes were transplanted into 6-week-old uPA-NOG hemizygous and homozygous recipients. The hepatocytes were successfully transplanted only into the homozygous uPA-NOG mice. Engraftment was demonstrated by different methods, including histology, human serum albumin measurements (ELISA), immunoblotting, and immunohistochemical staining (Fig. 3). At the time of transplantation, the recipient mice were clinically healthy and indistinguishable from non-transgenic uPA-NOG mice. Growth of transplanted human hepatocytes was not detectable in either the hemizygous or homozygous uPA-NOG mouse livers by gross inspection (Fig. 3A) because of the lack of obvious differences, such as color [8]. Periodic measurements of human albumin levels in the blood of each recipient were performed, to estimate repopulation of the mouse livers with human hepatocytes. Hemizygous recipients transplanted with human

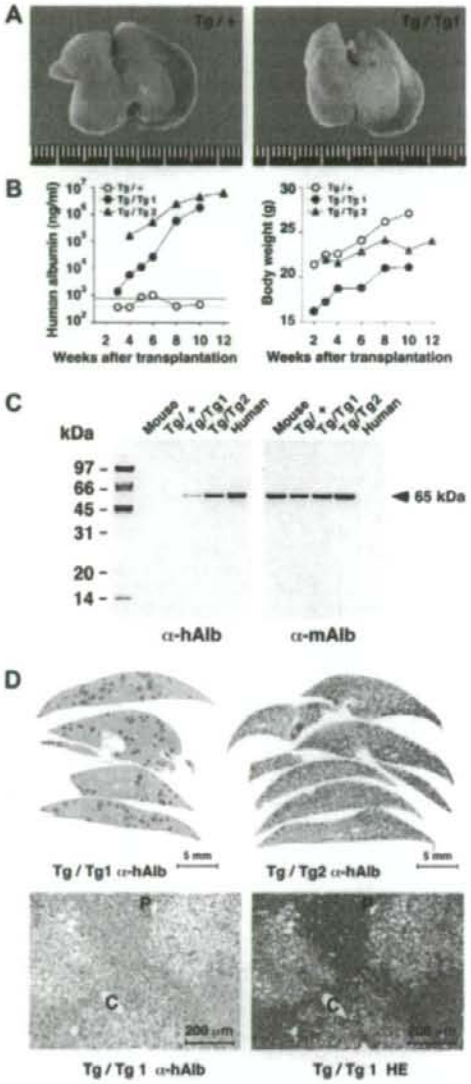

Fig. 3. Engraftment and repopulation of human hepatocytes in uPA-NOG mice. (A) Gross appearance of the uPA-NOG mouse liver 10 weeks after human hepatocyte transplantation. Tg/+, hemizygous; Tg/Tg, uPA-NOG homozygote. (B) Blood albumin concentrations in human cell recipients were assayed by ELISA. Dashed lines indicate the two standard deviation ranges for the values for the untransplanted uPA-NOG mice ($n = 6$). Body-weight changes after human hepatocyte transplantation are shown. (C) Immunoblot analysis shows human albumin (α-hAlb) and mouse albumin (α-mAlb) production in hemizygous (Tg/+) or homozygous (Tg/Tg) uPA-NOG transplant recipient mice. (D) Histology and immunohistochemistry of livers from uPA-NOG mice that were repopulated with human hepatocytes. Immunohistochemical staining for human albumin (top and lower left) and H&E staining (lower right). P, portal tract; C, central vein.

hepatocytes did not produce levels of human serum albumin that were indicative of a successful transplant (Fig. 3B, left); human albumin was not detected by immunoblotting (Fig. 3C, left) or

immunohistochemical staining (data not shown). Conversely, both homozygous recipients repopulated after transplantation of the human hepatocytes. These mice produced more than 1 mg/ml human albumin, and immunohistochemical staining suggested that the livers were comprised of at least 10–15% human hepatocytes (Fig. 3B, left). In one mouse, the circulating human serum albumin level continued to increase to 6.5 mg/ml. Although uPA-NOG hemizygotes and homozygotes both gained weight after transplantation (Fig. 3B, right), immunoblot analyses showed successful engraftment of the transplanted human hepatocytes in only the uPA-NOG homozygotes (Fig. 3C). Furthermore, human albumin was detected in the sera from both homozygotes (Tg/Tg1 and Tg/Tg2) with the anti-human albumin antibody; immunohistochemical staining for albumin further confirmed the human origin of these hepatocytes. Sera obtained from hemizygous uPA-NOG mice transplanted with human hepatocytes did not contain detectable amounts of human albumin. However, mouse albumin was detected in the sera from all of the mice.

Numerous mature human hepatocytes were identified in the livers of the transplanted uPA-NOG homozygotes (Fig. 3D, top). The number of human hepatocyte foci and the repopulation index, which was calculated based on the human hepatocyte/total liver cell number, appears to correspond to the measured blood levels of human albumin. In the Tg/Tg1 uPA-NOG homozygote, the blood human albumin levels reached 1.8 mg/ml, and the repopulation index was estimated to be 20% (Fig. 3D, upper and lower left). As mentioned previously, the human albumin levels reached 6.5 mg/ml in one mouse, a Tg/Tg2 uPA-NOG homozygote. In this mouse, almost 80% of the hepatocytes showed positive staining for human albumin, which suggests that the recipient liver was replaced by the transplanted human hepatocytes (Fig. 3D, top right). The human hepatocytes were fairly swollen and had a rarefied cytoplasm, such that these cells were easily discriminated from their murine counterparts (Fig. 3D, lower right). Periodic acid-Schiff (PAS) reaction showed that the empty spaces in these cells corresponded to areas of glycogen storage [22,23]. Furthermore, wisps and small clumps were evident in the cytoplasm, indicating that the organelles were displaced by excessive glycogen accumulation.

We anticipate that these humanized uPA-NOG mice will be useful for studying drug metabolism, general metabolic effects after hepatic engraftment, and the differentiation of stem cells for hepatocytes.

Acknowledgments

We thank Dr. R.D. Palmiter for providing plasmid p2335A-1, which carries the mouse albumin enhancer/promoter gene, S. Inoue, Y. Ando, M. Kuronuma, T. Mizushima, T. Kamisako, T. Etoh, and T. Ogura for their excellent technical assistance with animal experiments, C. Yagihashi and N. Omi for technical assistance with the molecular analyses, and Y. Ohnishi for helpful discussions. This work was supported by Grant-in-Aid for Scientific Research (17300136) as well as by Global COE Program for In vivo Human Metabolomic Systems Biology from MEXT.

References

[1] E.F. Brandon, C.D. Raap, I. Meijerman, J.H. Beijnen, J.H. Schellens, An update on in vitro test methods in human hepatic drug biotransformation research: pros and cons, Toxicol. Appl. Pharmacol. 189 (2003) 233–246.

[2] M.J. Gómez-Lechón, M.T. Donato, J.V. Castell, R. Jover, Human hepatocytes as a tool for studying toxicity and drug metabolism, Curr. Drug Metab. 4 (2003) 292–312.

[3] A.M. Yu, J.R. Idle, F.J. Gonzalez, Polymorphic cytochrome P450 2D6: humanized mouse model and endogenous substrates, Drug Metab. Rev. 36 (2004) 243–277.

[4] E.P. Sandgren, R.D. Palmiter, J.L. Heckel, C.C. Daugherty, R.L. Brinster, J.L. Degen, Complete hepatic regeneration after somatic deletion of an albumin-plasminogen activator transgene, Cell 66 (1991) 245–256.

[5] K.M. Braun, E.P. Sandgren, Liver disease and compensatory growth: unexpected lessons from genetically altered mice, Int. J. Dev. Biol. 42 (1998) 935–942.

[6] F.F. Mohammed, R. Khokha, Thinking outside the cell: proteases regulate hepatocyte division, Trends Cell Biol. 15 (2005) 555–563.

[7] J.A. Rhim, E.P. Sandgren, J.L. Degen, R.D. Palmiter, R.L. Brinster, Replacement of diseased mouse liver by hepatic cell transplantation, Science 263 (1994) 1149–1152.

[8] J.A. Rhim, E.P. Sandgren, R.D. Palmiter, R.L. Brinster, Complete reconstitution of mouse liver with xenogeneic hepatocytes, Proc. Natl. Acad. Sci. USA 92 (1995) 4942–4946.

[9] D.F. Mercer, D.E. Schiller, J.F. Elliott, D.N. Douglas, C. Hao, A. Rinfret, W.R. Addison, K.P. Fischer, T.A. Churchill, J.R. Lakey, D.L. Tyrrell, N.M. Kneteman, Hepatitis C virus replication in mice with chimeric human livers, Nat. Med. 7 (2001) 927–933.

[10] M. Dandri, M.R. Burda, E. Török, J.M. Pollok, A. Iwanska, G. Sommer, X. Rogiers, C.E. Rogler, S. Gupta, H. Will, H. Greten, J. Petersen, Repopulation of mouse liver with human hepatocytes and in vivo infection with hepatitis B virus, Hepatology 33 (2001) 981–988.

[11] K. Ohbo, T. Suda, M. Hashiyama, A. Mantani, M. Ikebe, K. Miyakawa, M. Moriyama, M. Nakamura, M. Katsuki, K. Takahashi, K. Yamamura, K. Sugamura, Modulation of hematopoiesis in mice with a truncated mutant of the interleukin-2 receptor gamma chain, Blood 87 (1996) 956–967.

[12] Y. Koyanagi, Y. Tanaka, J. Kira, M. Ito, K. Hioki, N. Misawa, Y. Kawano, K. Yamasaki, R. Tanaka, Y. Suzuki, Y. Ueyama, E. Terada, T. Tanaka, M. Miyasaka, T. Kobayashi, Y. Kumazawa, N. Yamamoto, Primary human immunodeficiency virus type 1 viremia and central nervous system invasion in a novel hu-PBL-immunodeficient mouse strain, J. Virol. 71 (1997) 2417–2424.

[13] M. Ito, H. Hiramatsu, K. Kobayashi, K. Suzue, M. Kawahata, K. Hioki, Y. Ueyama, Y. Koyanagi, K. Sugamura, K. Tsuji, T. Heike, T. Nakahata, NOD/SCID/gamma(c)(null) mouse: an excellent recipient mouse model for engraftment of human cells, Blood 100 (2002) 3175–3182.

[14] T. Yahata, K. Ando, Y. Nakamura, Y. Ueyama, K. Shimamura, N. Tamaoki, S. Kato, T. Hotta, Functional human T lymphocyte development from cord blood CD34+ cells in nonobese diabetic/Shi-scid, IL-2 receptor gamma null mice, J. Immunol. 169 (2002) 204–209.

[15] M. Ito, K. Kobayashi, T. Nakahata, NOD/Shi-scid IL2rgamma(null) (NOG) mice more appropriate for humanized mouse models, Curr. Top. Microbiol. Immunol. 324 (2008) 53–76.

[16] H. Masuda, T. Maruyama, E. Hiratsu, J. Yamane, A. Iwanami, T. Nagashima, M. Ono, H. Miyoshi, H.J. Okano, M. Ito, N. Tamaoki, T. Nomura, H. Okano, Y. Matsuzaki, Y. Yoshimura, Noninvasive and real-time assessment of reconstructed functional human endometrium in NOD/SCID/gamma c(null) immunodeficient mice, Proc. Natl. Acad. Sci. USA 104 (2007) 1925–1930.

[17] R. Matsuura-Sawada, T. Murakami, Y. Ozawa, H. Nabeshima, J. Akahira, Y. Sato, Y. Koyanagi, M. Ito, Y. Terada, K. Okamura, Reproduction of menstrual changes in transplanted human endometrial tissue in immunodeficient mice, Hum. Reprod. 20 (2005) 1477–1484.

[18] C.A. Pinkert, D.M. Ornitz, R.L. Brinster, R.D. Palmiter, An albumin enhancer located 10 kb upstream functions along with its promoter to direct efficient, liver-specific expression in transgenic mice, Genes Dev. 1 (1987) 268–276.

[19] C. Maruyama, H. Suemizu, S. Tamamushi, S. Kimoto, N. Tamaoki, Y. Ohnishi, Genotyping the mouse severe combined immunodeficiency mutation using the polymerase chain reaction with confronting two-pair primers (PCR-CTPP), Exp. Anim. 51 (2002) 391–393.

[20] E.P. Sandgren, R.D. Palmiter, J.L. Heckel, R.L. Brinster, J.L. Degen, DNA rearrangement causes hepatocarcinogenesis in albumin-plasminogen activator transgenic mice, Proc. Natl. Acad. Sci. USA 89 (1992) 11523–11527.

[21] J.L. Heckel, E.P. Sandgren, J.L. Degen, R.D. Palmiter, R.L. Brinster, Neonatal bleeding in transgenic mice expressing urokinase-type plasminogen activator, Cell 62 (1990) 447–456.

[22] P. Meuleman, L. Libbrecht, R. De Vos, B. de Hemptinne, K. Gevaert, J. Vandekerckhove, T. Roskams, G. Leroux-Roels, Morphological and biochemical characterization of a human liver in a uPA-SCID mouse chimera, Hepatology 41 (2005) 847–856.

[23] H. Azuma, N. Paulk, A. Ranade, C. Dorrell, M. Al-Dhalimy, E. Ellis, S. Strom, M.A. Kay, M. Finegold, M. Grompe, Robust expansion of human hepatocytes in Fah−/−/Rag2−/−/Il2rg−/− mice, Nat. Biotechnol. 25 (2007) 903–910.

Int. J. Cancer: 124, 622–629 (2009)

An HIV protease inhibitor, ritonavir targets the nuclear factor-kappaB and inhibits the tumor growth and infiltration of EBV-positive lymphoblastoid B cells

Md. Zahidunnabi Dewan[1,2], Mariko Tomita[3], Harutaka Katano[4], Norio Yamamoto[1], Sunjida Ahmed[1], Michiko Yamamoto[5], Tetsutaro Sata[4], Naoki Mori[3]* and Naoki Yamamoto[1,2]*

[1]*Department of Molecular Virology, Graduate School, Tokyo Medical and Dental University, 1-5-45 Yushima, Bunkyo-ku, Tokyo 113-8519, Japan*
[2]*AIDS Research Center, National Institute of Infectious Diseases, 1-23-1 Toyama, Shinjuku-ku, Tokyo 162-8640, Japan*
[3]*Division of Molecular Virology and Oncology, Graduate School of Medicine, University of the Ryukyus, 207 Uehara, Nishihara, Okinawa 903-0215, Japan*
[4]*Department of Pathology, National Institute of Infectious Diseases, 1-23-1 Toyama, Shinjyuku-ku, Tokyo 162-8640, Japan*
[5]*Division of Safety Information on Drug, National Institute of Health Sciences, Food and Chemicals, Setagaya-ku, Tokyo 158-8501, Japan*

Epstein-Barr Virus (EBV)-associated immunoblastic lymphoma occurs in immunocompromised patients such as those with AIDS or transplant recipients after primary EBV infection or reactivation of a preexisting latent EBV infection. In the present study, we evaluated the effect of ritonavir, an HIV protease inhibitor, on EBV-positive lymphoblastoid B cells ***in vitro*** and in mice model. We found that it induced cell-cycle arrest at G_1-phase and apoptosis through down-regulation of cell-cycle gene cyclin D2 and anti-apoptotic gene survivin. Furthermore, ritonavir suppressed transcriptional activation of NF-jB in these cells. Ritonavir efficiently prevented growth and infiltration of lymphoma cells in various organs of NOD/SCID/cc^{null} mice at the same dose used for treatment of patients with AIDS. Our results indicate that ritonavir targets NF-jB activated in tumor cells and shows anti-tumor effects. These data also suggest that this compound may have promise for treatment or prevention of EBV-associated lymphoproliferative diseases that occur in immunocompromised patients.
© 2008 Wiley-Liss, Inc.

Key words: ritonavir; LCLs; NF-jB; NOG mice

Epstein-Barr virus (EBV) is a ubiquitous human g herpes virus that establishes a latent infection more than 90% of adults worldwide.[1] Immunocompromised individuals such as those with AIDS or transplant recipients are at increased risk for developing aggressive EBV-associated lymphoproliferative diseases. EBV is associated with malignant diseases, including Burkitt's lymphoma,[1,2] nasopharyngeal carcinoma[3,4] and immunoblastic B cell lymphoma of immunosuppressed individuals. Infection of primary B cells with EBV results in transformation with growth of the cells in tight clumps and immortalization of the cells. These immortalized B cells have an immunoblastic morphology and express each of the EBV-encoded small RNAs (EBERs), EBV nuclear antigen (EBNAs) and latent membrane proteins (LMPs).[2,5] EBERs have oncogenic potential through inhibition of PKR.[6] EBNA-2 is a transactivator that up-regulates expression of cellular genes and LMPs. LMP-1 may mediate proliferative and survival effects not only in EBV-transformed B lymphocytes but also in these malignancies that occur long after primary infection. Many immunocompromised patients with EBV-associated immunoblastic lymphoma have tumors at extranodal sites such as the brain, lung, or gastrointestinal tract. The prognosis of EBV-associated lymphomas is very poor for patients with irreversible immunosuppression and treatment options are limited.

Despite the diversity in clinical manifestations of hematopoietic malignancies, strong and constitutive nuclear factor-kappaB (NF-jB) activation was reported to be a unique and common characteristic of malignant cells.[7,8] In resting cells, NF-jB is sequestered as an inactive precursor by association with inhibitory IjBs in the cytoplasm. On stimulation, IjBs are rapidly phosphorylated, ubiquitinated and degraded by a proteasome-dependent pathway allowing active NF-jB to translocate into the nucleus where it can activate the expression of a number of genes.[9] LMP-1 is an oncoprotein that constitutively activates NF-jB to induce B cell proliferation.[7] Lymphoblastoid cell lines (LCLs) express high level of the antiapoptotic proteins BCL-2, BCL-xL, c-IAP1, Bfl-1 and c-FLIP the targets of NF-jB.[10,11] NF-jB activation has been connected with multiple processes of oncogenesis including control of apoptosis, cell-cycle, differentiation and cell migration,[9] and therefore, inhibition of NF-jB was suggested to be a useful strategy for cancer therapy.[12–20] It has been also reported that inhibition of NF-jB in EBV-associated lymphomas results in induction of apoptosis.[21] Therefore, targeting the NF-jB pathway and inhibition of NF-jB activity is a logical strategy for treating EBV-associated lymphomas.

Ritonavir, a human immunodeficiency virus type 1(HIV-1) protease inhibitor, has been successfully used in clinical treatments of HIV infection, with patients exhibiting a marked decrease in HIV viral load and a subsequent increase in CD4[1] T-cell counts.[22–25] Evidence of other effects by ritonavir on cellular proteases, such as the cysteine proteases cathepsin D and E, was presented in the drug's original description, albeit at concentrations >500-fold above the concentration required for inhibition of HIV protease.[26] Protease inhibitors have also been shown to directly affect cell metabolism, interfere with host or fungal proteases and block T-cell activation and dendritic-cell function.[27,28] Ritonavir has been shown to inhibit the chymotrypsin-like activity of the 20S proteasome, and it activates the chymotrypsin-like activity of the 26S proteasome conversely.[27,29,30] Ritonavir also has been reported to inhibit the transactivation of NF-jB induced by activators such as TNFa, HIV-1 Tat protein and the human herpesvirus 8 protein ORF74.[31] It is possible that inhibition of NF-jB activation by ritonavir is linked to additional pathways other than inhibition of proteasome.[31] Protease inhibitors also have been shown to have direct antiangiogenic and antitumor activity.[31,32] Recently, we reported that ritonavir inhibits growth and infiltration of ATL cells through targeting NF-jB.[20]

Grant sponsors: Ministry of Education, Science and Culture, The Ministry of Health, Labor and Welfare, Human Health Science of Japan.
Md. Zahidunnabi Dewan's current address is: Department of Pathology, New York University School of Medicine, 550 First Avenue, New York, NY 10016, USA.
Md. Zahidunnabi Dewan and Mariko Tomita contributed equally to this work.
*Correspondence to: AIDS Research Center, National Institute of Infectious Diseases, 1-23-1 Toyama, Shinjuku-ku, Tokyo 162-8640, Japan. Fax: 8135-285-1165. E-mail: nyama@nih.go.jp (or) Division of Molecular Virology and Oncology, Graduate School of Medicine, University of the Ryukyus, 207 Uehara, Nishihara, Okinawa 903-0215, Japan. Fax: 81-98-895-1410. E-mail: n-mori@med.u-ryukyu.ac.jp.
Received 14 July 2008; Accepted after revision 2 September 2008
DOI 10.1002/ijc.23993
Published online 15 September 2008 in Wiley InterScience (www.interscience.wiley.com).

In the present, we demonstrate that inhibition of NF-jB activity by ritonavir results in marked increase of apoptosis and induce cell-cycle arrest in EBV-positive lymphoblastoid B cells. We found that ritonavir also suppresses the expression of genes involved in antiapoptosis and cell-cycle progression. In addition, we established preclinical models using newly developed NOD/SCID/gc^{null} (NOG) mouse,[16] a unique type of animal, lacking T-, B- and NK-cells to evaluate the efficacy of antitumor and anti-NF-jB therapies. In the murine model, ritonavir at the clinically relevant dose potently inhibited the growth and infiltration of EBV-transformed LCL cells.

Material and methods

Mice and cells

NOG mice were obtained from the Central Institute for Experimental Animals (Kawasaki, Japan). All mice were maintained under specific-pathogen-free conditions in the Animal Center of Tokyo Medical and Dental University (Tokyo, Japan). The Ethical Review Committee of the Institute approved the experimental protocol.

EBV-positive immortalized lymphoblatoid B-cell lines (LCL-Ya, LCL-Ao, LCL-Ka and LCL-Ku) were cultured in RPMI 1640 medium supplemented with 10% heat-inactivated fetal bovine serum (JRH Biosciences, Lenexa, KS), 100 U/ml penicillin, and 10 lg/ml streptomycin. Peripheral blood mononuclear cells (PBMCs) from 3 healthy volunteers were analyzed. Mononuclear cells were isolated by Ficoll-Paque density gradient centrifugation (GE Healthcare Biosciences, Uppsala, Sweden) and washed with PBS.

Cell viability assay

The effect of ritonavir on cell viability of LCLs and PBMCs from healthy donors was examined by the reagent, water-soluble tetrazolium (WST)-8 (Wako Chemicals, Osaka, Japan). Briefly, 2 3 10^5 cells were incubated in a 96-well microculture plate in the absence or presence of various concentrations of ritonavir. After 72 hr of culture, WST-8 (5 ll) was added for the last 4 hr of incubation and absorbance at 450 nm was measured using an automated microplate reader. Measurement of mitochondrial dehydrogenase cleavage of WST-8 to formazan dye provides an indication of the level of cell viability.[*]

Cell-cycle analysis

Cells were plated at a density of 3 3 10^5/ml in 60-mm tissue culture dishes. Twelve hours after plating, cells were exposed to 40 lM ritonavir for 24 h. Cell-cycle analysis was performed with the CycleTEST PLUS DNA reagent kit (Becton Dickinson, San Jose, CA). Briefly, cells were washed with a buffer solution containing sodium citrate, sucrose and dimethyl sulfoxide, suspended in a solution containing RNase A, and stained with 125 lg/ml propidium iodide (PI) for 10 min. Cell suspensions were analyzed on EPICS XL flow cytometer (Beckman Coulter, Fullerton, CA) using EXPO32 software. The cell population at each cell-cycle phase was determined with MultiCycle software (Beckman Coulter).

Assay for apoptosis

Cells were plated at a density of 3 3 10^5/ml in 60-mm tissue culture dishes. Twelve hours after plating, cells were exposed to ritonavir for 72 hr. Apoptosis was quantified by double staining with Annexin-V-Fluos (Roche Diagnostics, Mannheim, Germany) and PI (Backman Coulter) according to the instructions supplied by the manufacturer. Cells were analyzed on EPICS XL flow cytometer (Beckman Coulter) using EXPO32 software.

Western blot analysis

Treated cells were solubilized at 4 C in lysis buffer containing 62.5 mM Tris-HCl (pH 6.8), 2% SDS, 10% glycerol, 6% 2-mercaptoethanol and 0.01% bromophenol blue. Samples were subjected to electrophoresis on SDS-polyacrylamide gels followed by transfer to a polyvinylidine difluoride membrane and probing with the following specific antibodies: polyclonal antibodies against survivin, cyclin D2 (Santa Cruz Biotechnology, Santa Cruz, CA), Bcl-X_L (BD Transduction Laboratories, San Jose, CA) and monoclonal antibodies against Bcl-2, p53, actin (NeoMarkers, Fremont, CA), PARP (BD Transduction Laboratories) and LMP-1 (DAKO, Kyoto, Japan). The protein bands recognized by the antibodies were visualized using the enhanced chemiluminescence system (Amersham, Piscataway, NJ).

Electrophoresis mobility shift assay (EMSA)

Cells were placed in culture at 1 3 10^6 cells/ml and examined for inhibition of NF-jB 24 hr after exposure to ritonavir. Nuclear proteins were extracted, and NF-jB binding activities to jB element were examined by EMSA as described previously.[8] In brief, 5 lg of nuclear extracts were preincubated in a binding buffer containing 1 lg of poly (dI:dC) (Amersham Biosciences), followed by addition of ^{32}P-labeled oligonucleotide probe containing NF-jB element (5 3 10^4 c.p.m.). These mixtures were incubated for 15 min at room temperature. The DNA-protein complexes were separated on a 4% polyacrylamide gel and visualized by autoradiography. To examine the specificity of the NF-jB element probe, unlabeled competitor oligonucleotides were preincubated with nuclear extracts for 15 min before incubation with probes. The probe or competitors used were prepared by annealing the sense and antisense synthetic oligonucleotides as follows: a typical NF-jB element from the *IL-2Ra* gene, 5'-gatcCGGCAGGGGAATCTCCCTCTC-3'; and AP-1 element of the *IL-8* gene, 5'-gactGTGATGACTCAGGTT-3'. Underlined sequences represent the NF-jB or AP-1 binding site. To identify NF-jB protein in the DNA protein complex revealed by EMSA, we used antibodies specific for various NF-jB proteins, including p50, p65, c-Rel, RelB and p52 (Santa Cruz Biotechnology), to elicit a supershift DNA protein complex formation. These antibodies were incubated with the nuclear extracts for 45 min at room temperature before incubation with radiolabeled probes.

Inoculation of EBV-positive immortalized LCLs and collection of samples

LCL Cells [LCL-Ya, LCL-Ao, LCL-Ka and LCL-Ku] were washed twice with serum-free RPMI-1640 medium and resuspended in same medium. Mice were anaesthetized with ether and cells were inoculated subcutaneously (sc) in the postauricular region of NOG mice at a dose of 1 3 10^7 cells per mouse. All mice were sacrificed 3 weeks after inoculation with lymphoma cells. We measured tumor size 3 weeks after inoculation. Tissues and various organs of mice were collected and fixed with Streck Tissue Fixative, then processed to paraffin wax-embedded sections for staining with hematoxylin and eosin (HE) and immunostaining.

PCR primer and conditions

Detection of the BamHI W repeat region of the EBV genome was performed using 100 ng of genomic DNA extracted from LCLs as follows. LCLs were lysed with genomic DNA extraction buffer (100 mM Tris-HCl pH8.0, 5 mM EDTA, 0.2% SDS, 200 mM NaCl and 200 lg/mL proteinase K) and the lysate was incubated at 50 C for 3 hr. After phenol-chloroform extraction, genomic DNA was purified by ethanol precipitation procedure. A 121-bp fragment of the EBV W repeat region was amplified by the forward primer 5'-CGCATAATGGCGGACCTAG-3' and reverse primer 5'-CAAACAAGCCCACTCCCC-3' in a 25 ll reaction mixture comprising 1 3 AmpliTaq Gold buffer, 3.5 mM MgCl2, 200 lM dNTP, 300 nM primers, 200 nM probe and 0.025 U/ll AmpliTaq Gold. The PCR cycle conditions were as follows: a DNA denaturation and polymerase activation step of 10 min at 95 C and then 40 cycles of amplification (95 C for 15 sec, 60 C for 1 min). PCR products were separated by electrophoresis on agarose gels, stained with ethidium bromide and visualized by UV-light.

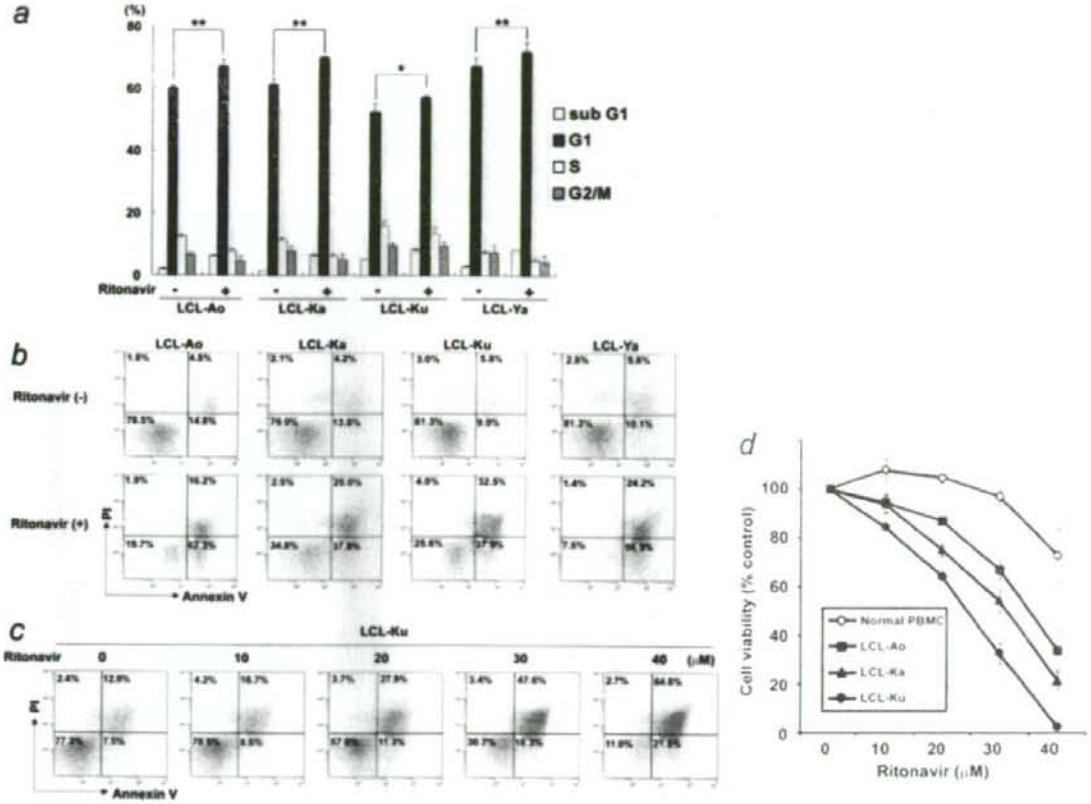

FIGURE 1 – Effect of ritonavir on cell cycle arrest and induction of apoptosis of EBV-positive lymphoblastoid B cells. (*a*) Effect of ritonavir on cell cycle progression of EBV-positive lymphoblastoid B cells. Cells were cultured for 24 hr with (1) or without (2) ritonavir (40 IM). DNA content was analyzed by flow cytometry with PI staining. Sub G_1, S and G_2/M indicate the stages of the cell cycle. Data are expressed as the mean percentages of the cells from three independent experements. Significance of differences between % G_1 of ritonavir treated (1) and untreated (2) cells calculated by Student's *t*-test is shown as *P*-value with astalisk(s). $^*p < 0.05$ and $^{**}p < 0.01$. (*b*) Effect of ritonavir on induction of apoptosis of EBV-immortalized B-cell lines. Cells were cultured for 72 hr with (1) or without (2) ritonavir (40 IM). (*c*) Ritonavir induces apoptosis of EBV-immortalized B-cell lines in a dose-dependent manner. LCL-Ku cells were cultured for 72 hr with increasing concentration of ritonavir (0, 10, 20, 30, 40 IM). Cells were harvested and stained with Annexin-V and PI. Apoptosis was analyzed by flow cytometry. Bottom left quadrants, viable cells; bottom right quadrants, early apoptotic cells. Top right quadrants, nonviable, late apoptotic/necrotic cells. (*d*) Effect of ritonavir on cell viability of LCLs and PBMCs from normal healthy controls. LCLs and PBMCs were incubated in the presence of various concentrations of ritonavir for 72 hr and viability of the cultured cells was measured by WST-8 assay. Relative viability of the cultured cells is presented as the mean determined on LCLs and PBMCs from triplicate cultures. A relative viability of 100% was designated as total number of cells that grew in 72-hr cultures in the absence of ritonavir.

Treatment of tumor-bearing mice with ritonavir

Ritonavir was obtained from Abbott Labs, North Chicago, IL. LCL-Ku cells (1 3 10^7) were inoculated s.c. in the post-auricular region of NOG mice. The drug was administered s.c. into the tumor cells inoculated site of mice at doses of 30 mg/kg/day, beginning on day 0 for 3 weeks. The control mice received RPMI-1640 (200 II) simultaneously. In other experiments, ritonavir or RPMI-1640 was also administered intraperitoneally into mice as the same doses stated above, beginning on day 4 for 18 days.

In situ *hybridization*

EBERs were detected by *in situ* hybridization using fluorescein isothiocyanate (FITC)-conjugated EBER PNA (peptide nucleic acid)-probe (DAKO). Briefly, formalin-fixed, paraffin-embedded tissue sections of tumor and various organs were deparaffinized and hydrated in xylenes and graded alcohol series, then rinsed for 5 min in PBS. Deparaffinized samples were incubated with 10 ng/II of proteinase K for 20 min at 37 C followed by washing, and then incubated with 0.3% methanol for 30 min at room temperature. After washing in PBS, the sections were hybridized with FITC-conjugated EBER-PNA probe in the hybridization solution for 90 min at 56 C. The slides were washed twice in 0.2 3 SSC for 20 min at 56 C, and incubated with anti-FITC monoclonal antibody (DAKO) for 45 min at 37 C. Followed by washing, the slides were incubated with horse-radish peroxidase-conjugated polymer reagent (Envision, DAKO) for 30 min at room temperature. Positive staining was visualized after incubation of these samples with a mixture of 0.05% 3,3'-diaminobenzidine tetrahydrochloride in 50 mM Tris-HCl buffer pH7.6 and 0.01% hydrogen peroxide for 5 min. The samples were counterstained with hematoxlin for 2 min, hydrated completely, cleaned in xylene and then mounted. The samples were visualized and photographed under light microscopy (BX41 and DP70; Olympus, Tokyo, Japan).

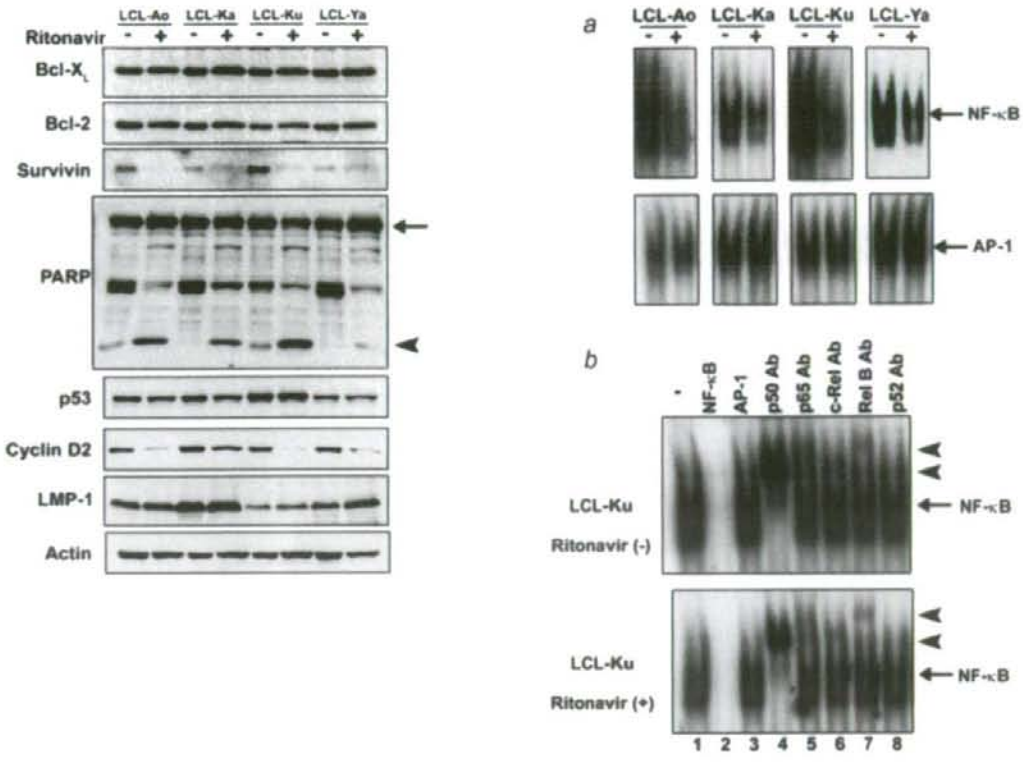

FIGURE 3 – Ritonavir inhibits constitutive NF-jB activation. (*a*) EBV-immortalized B-cell lines were cultured with (1) or without (2) ritonavir (40 IM) for 24 hr and assessed for NF-jB and AP-1-DNA binding activity. (*b*) Cold competition using 100-fold excess of unlabeled NF-jB oligonucleotide, or AP-1 oligonucleotide (lanes 2–3) demonstrated the specificity of the protein/DNA binding complexes. Specificity of NF-jB binding was also determined by using antibodies to the NF-jB components p50, p65, c-Rel, RelB and p52, resulting in supershift (lanes 4–8). Arrows indicate specific complexes of NF-jB with wild type NF-jB oligonucleotide. Arrow heads indicate supershift. Essentially the same results were obtained in 3 experiments and representative data are shown.

Results

Ritonavir induces cell-cycle arrest and apoptosis of LCLs

Ritonavir was examined for its effect on cell-cycle distribution of EBV-immortalized LCLs (Fig. 1*a*). Ritonavir effectively inhibited cell-cycle progression, as evidenced by increased proportion of the cells in G_1 phase of LCL-Ao, LCL-Ka, LCL-Ku and LCL-Ya (LCL-Ao: from 60.1% to 67.1%; LCL-Ka: from 61.2% to 69.9%; LCL-Ku: from 52.6% to 57.3%; and LCL-Ya: from 67.4% to 72.1%). These results indicated that ritonavir induced cell-cycle arrest at G_1-phase. The weak accumulation of cells in G_1 phase by ritonavir suggests that it might rather be an apoptosis inducer than a cell growth inhibitor.

Furthermore, we evaluated the effect of ritonavir on the cell viability of LCLs and PBMCs from healthy individuals (Fig. 1*d*). Ritonavir effectively reduced the survival of LCLs (LCL-Ao, LCL-Ka and LCL-Ku) as measured by WST-8 on the third day of culture in a dose-dependent manner. In contrast, ritonavir hardly affected the survival of PBMCs from healthy volunteers.

The effect of ritonavir on apoptosis was examined by the Annexin-V and PI method. Annexin-V binds to the cells that express phosphatidylserine on the outer layer of the cell membrane, a characteristic feature of cells entering apoptosis. Early apoptotic cells were stained with Annexin V but not with PI. Late apoptotic and necrotic cells were stained with both fluorescent. Ritonavir induced increased proportion of cells positive for Annexin-V and negative for PI in all cell lines (LCL-Ao: from 14.8% to 62.3%; LCL-Ka: from 13.8% to 37.8%; LCL-Ku: from 9.9% to 37.9% and LCL-Ya: from 10.1% to 66.9%) (Fig. 1*b*). Ritonavir also induced dose-dependent increasing of Annexin-V positive and PI negative cells in LCL-Ku cells (Fig. 1*c*), indicating increasing apoptosis of ritonavir-treated cells.

Ritonavir down-regulates the expression of the cell-cycle- and apoptosis-associated genes

The antiproliferative and proapoptotic effects of ritonavir were explored by examining the levels of intracellular regulators of cell-cycle and apoptosis after exposure to ritonavir (Fig. 2). Ritonavir down-regulated the levels of survivin and cyclin D2 in EBV-immortalized B-cell lines. We also observed increased cleavage of PARP in these cells. However, ritonavir did not modulate the other regulators of cell-cycle and apoptosis such as Bcl-X_L, Bcl-2 and p53. Ritonavir had no effect on the expression of viral proteins such as LMP-1, suggesting that ritonavir may induce cell-cycle arrest and apoptosis by down-regulating the levels of survivin and cyclin D2 without reducing the virus levels in the cells.

Ritonavir suppresses constitutive NF-jB expressed by EBV-transformed LCLs

To examine the effect of ritonavir on NF-jB DNA binding, EMSA was performed. EBV-immortalized B-cell lines were incubated with or without 40 IM ritonavir for 24 h, and nuclear extracts were prepared and examined for NF-jB by EMSA.

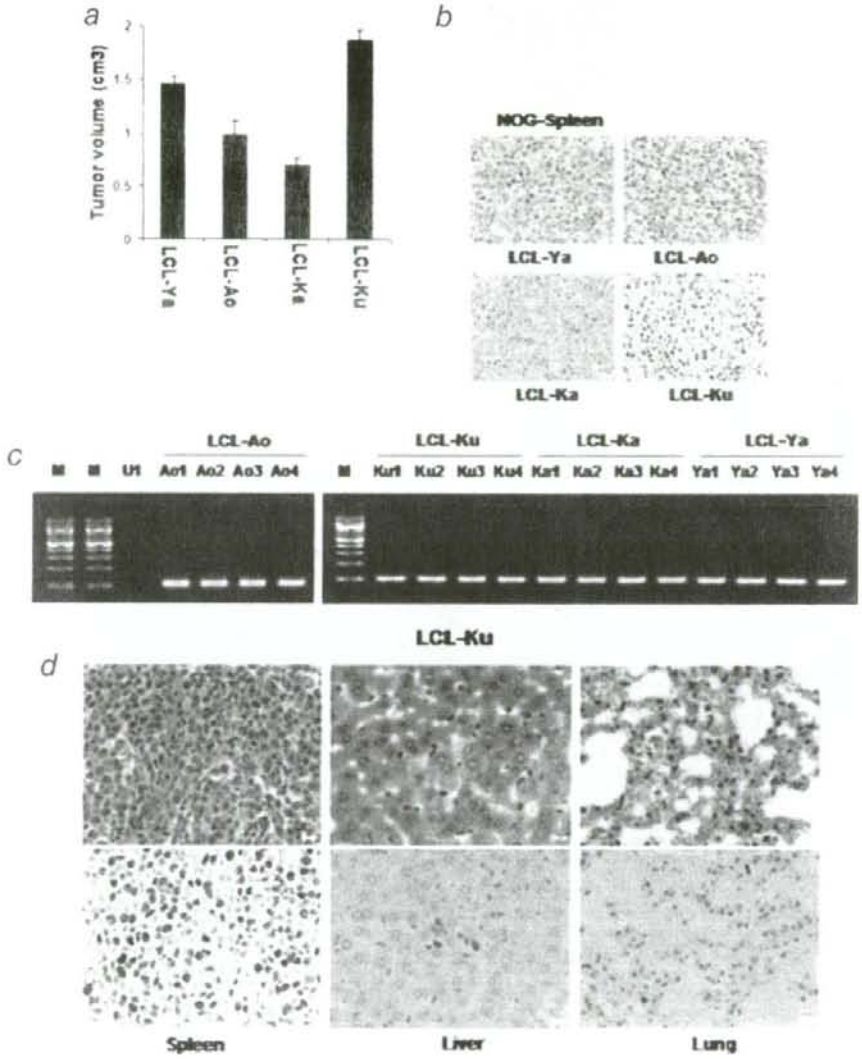

FIGURE 4 – Successful engraftment and infiltration of EBV-positive lymphoblastoid B cells in NOG mice. (*a*) Subcutaneous tumor size in mice 21 days after inoculation with various LCL cells. (*b*) *In situ* hybridization for EBER of spleen from NOG mice not receiving tumor cells, as a negative control and tumor tissues of LCL cells injected mice. Magnification 340. (*c*) Detection of viral DNA by PCR. M, Marker; U1; EBV-negative U937 cell for negative control; Ao1, *in vitro* culture and Ao2, Ao3 and Ao4, *in vivo* samples from 3 different mice inoculated with LCL-Ao; Ku1, *in vitro* culture and Ku2, Ku3 and Ku4, *in vivo* sample from 3 different mice inoculated with LCL-Ku; Ka1, *in vitro* culture and Ka2, Ka3 and Ka4, *in vivo* sample from 3 different mice inoculated with LCL-Ka, Ya1, *in vitro* culture and Ya2, Ya3 and Ya4, *in vivo* sample from 3 different mice inoculated with. LCL-Ya. Infiltration of EBV-immortalized B-cell lines in various organs of NOG mice. (*d*) HE and *in situ* hybridization for EBER of spleen, liver and lung of mice inoculated with LCL-Ku cells. Left, middle and right panels represent spleen, liver and lung, respectively. Upper and lower panels represent HE and EBER, respectively (magnification 340).

Down-regulation of NF-jB occurred in all cell lines (Fig. 3*a*, upper panels). Inhibition appeared specific to NF-jB, because no significant change in binding activity of AP-1 was observed after treatment of cells with ritonavir (Fig. 3*a*, lower panels). Also, the observed protein/DNA binding was specific for NF-jB, because the binding was effectively competed and abrogated by excess unlabeled NF-jB oligonucleotide but not by mutant NF-jB or AP-1 oligonucleotide (Fig. 3*b*). LCL-Ku cell extract without ritonavir treatment contained p50, p65 and Rel B proteins in the NF-jB complex (Fig. 3*b*, upper panel), and ritonavir did not affect components of the NF-jB complex (Fig. 3*b*, lower panel).

Efficient engraftment and infiltration of EBV-transformed LCLs in NOG mice

EBV-immortalized LCLs (LCL-Ya, LCL-Ao, LCL-Ka and LCL-Ku) were inoculated s.c. in the post-auricular region of NOG mice (Fig. 4 and Table I). Mice inoculated with LCL cells (LCL-

TABLE I – *IN VIVO* CHARATERISTICS OF EBV-POSITIVE LYMPHOBLASTOID B CELLS IN NOG MICE

Cell line	Orgin/EBV status	No. of cells inoculated/mouse (10^7)[1]	Inoculation route[2]	Day of sacrifice after inoculation	No. of mice with tumor/no. of mice inoculated[3]	Organ-infiltration[4]		
						Spleen	Liver	Lung
LCL-Ya	B/1	1	sc	21	03/03	1 1	2	2
LCL-Ao	B/1	1	sc	21	03/03	1 1	2	2
LCL-Ka	B/1	1	sc	21	03/03	1 1	2	2
LCL-Ku	B/1	1	sc	21	21/21	1 1 1	1	1

[1]Mice were inoculated with 1 3 10^7 cells per mouse.–[2]sc, subcutaneous.–[3]Number of animals in which tumor developed.–[4]Organ-infiltration was examined by histological analysis. 2, no infiltration; 1, slight infiltration; 1 1, marked infiltration; 1 1 1, massive infiltration.

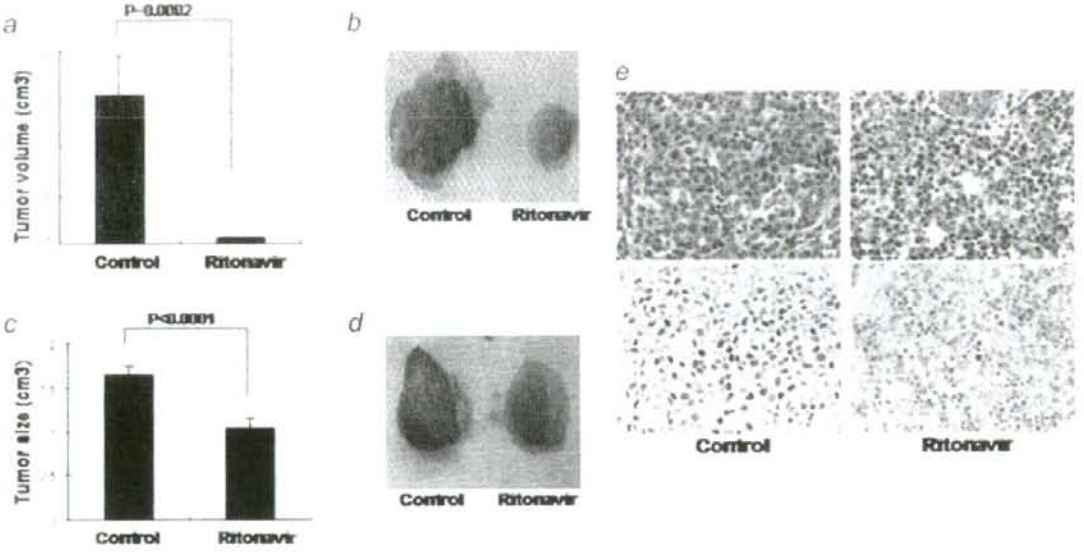

FIGURE 5 – Effect of ritonavir on lymphoma cell growth and infiltration. Mice were injected with LCL-Ku cells (1 3 10^7 cells) s.c. in the postauricular region. (*a* and *b*) The drug was administered s.c. into the tumor cells inoculated site of mice at doses of 30 mg/kg/day, beginning on day 0 for 3 weeks. The control mice received RPMI-1640 (200 l) simultaneously. (*a*) Average size of tumor, data represent the mean 6 SD from 6 mice. (*b*) Photograph of subcutaneously formed excised tumor without (left) and with (right) ritonavir treatment. (*c* and *d*) Effect of ritonavir on established tumor, ritonavir or RPMI-1640 was also administered intraperitoneally into mice as the same doses stated above, beginning on day 4 for 18 days. (*c*) Average size of tumor, data represent the mean 6 SD from 6 mice. (*d*) Photograph of subcutaneously formed excised tumor without (left) and with (right) ritonavir treatment. (*e*) HE and *in situ* hybridization for EBER in spleen tissue of LCL cells injected mice. Magnification 340. Upper and lower panels show HE and EBER staining, respectively.

Ya, LCL-Ao, LCL-Ka and LCL-Ku) produced a visible tumor within 3 weeks in all NOG mice. LCL-Ku cell was very efficient in the formation of a large tumor (Fig. 4*a*), as well as development of clinical signs of near-death, such as pilorection, weight loss and cachexia in mice at the time point of sacrifice. The average tumor size (LCL-Ya, LCL-Ao, LCL-Ka and LCL-Ku) in NOG mice inoculated s.c. with lymphoma cells was shown in Figure 4*a*. To test whether tumors maintain original histomorphology and expression patterns of tumor markers in NOG, we performed HE and *in situ* hybridization for EBER of normal mice spleen not receiving tumor cells and tumor tissues obtained from mice inoculated with LCLs. Histological analysis revealed that morphologically immunoblastic cells with large nucleus, clear nuclear membrane and broad cytoplasm expressed EBER, whereas EBER was not detected in spleen tissue collected from mice not receiving tumor cells, suggesting that *in vivo* tumor cells preserved well morphology as well as expressed viral gene EBER (Fig. 4*b*). Tumor cells from mice inoculated with EBV-immortalized B-cell lines were positive for DNA of EBV by PCR (Fig. 4*c*). These results showed that EBV-immortalized B-cell lines inoculated s.c. into the postauricular region of NOG mice were able to produce a visible tumor very efficiently. To assess the tissue distribution of lymphoma cells, we carried out histological examinations of the different organs of NOG mice after inoculation of the cells. Proliferation and infiltration of tumor cells were found not only in primary tumor tissues but also in spleen and to a lesser extent in liver and lung of NOG mice inoculated with tumor cells (Table I). HE and *in situ* hybridization staining for EBER showed a degree of infiltration of tumor cells at the site of inoculation and various organs with lymphoma cells (Fig. 4*d*). Interestingly, LCL-Ku cells appeared to infiltrate in various organs of mice more aggressively and massively than other cells. This extremely rapid tumor formation and infiltration in all mice is one of the hallmarks of our clinically relevant animal model without change of histomorphology or tumor marker expression.

Ritonavir suppresses the LCLs growth and infiltration in vivo

To determine the effect of ritonavir on tumor growth and infiltration, we injected LCL-Ku cells (1 3 10^7) s.c. into the postauricular region of NOG mice. Mice were treated with either RPMI-1640 (as control) or ritonavir (30 mg/kg/day), beginning on either day 0 or day 4. A significant decrease in the size of tumors in mice treated with ritonavir was demonstrated when compared with controls 3 weeks after the injection of tumor cells (Fig. 5*a*). Gross appearance of the mice treated by ritonavir showed apparent

reduction of the tumor mass at 3 weeks after inoculation of tumor cells (Fig. 5*b*). Ritonavir also inhibited the size and growth of established tumors (Fig. 5*c* and 5*d*). Ritonavir at this treatment dosage (30 mg/kg/day for 3 weeks) is well tolerated without adverse findings such as standing of hair, weight loss and cachexia of treated mice, all of which are signs of near death. Clinical evaluation of organ invasion 3 weeks after injection of tumor cells showed that ritonavir treatment inhibited their infiltration into spleen (Fig. 5*e*). In contrast, all control mice showed infiltration with tumor cells into spleen. Organ infiltration of lymphoma cells were analyzed and evaluated by HE and *in situ* hybridization of EBER. Together, these data indicate that ritonavir significantly inhibits lymphoma cell growth and infiltration in various organs of NOG mice (Fig. 5).These results suggest that ritonavir contributes to the reduction of the tumor growth and inhibits the organ infiltration in the mice through targeting the constitutive NF-jB activity.

Discussion

EBV-positive malignancies in immunocompromised patients are associated with high mortality and reduce overall survival period. The various chemotherapies so far developed have not increased significantly the survival of patients with EBV-associated malignancies in immunocompromised patients. Given disappointing results using conventional chemotherapy, new treatment strategies that specially target EBV-transformed cells are need.[1,2] LMP-1 is an oncogene that constitutively activates NF-jB to induce B cell proliferation.[7] It has been previously reported that suppression of high NF-jB activity inhibited cell growth and induced apoptosis of cancer cells as well as EBV-transformed cells both *in vitro* and *in vivo*.[12–20,33] Ritonavir is cytotoxic for different types of malignant cells *in vitro* through affecting proteasomal proteolysis, although concentrations necessary to show the *in vitro* effect exceed the achievable therapeutic drugs level.[27,29,30] It may affect the stabilization of p21, p27 and p53 proteins. Recently, ritonavir has been shown to inhibit NF-jB activity and induce the apoptosis of ATL cells.[20] This led us to investigate whether this drug exhibits anti-tumor effects against EBV-transformed cells *in vitro* and in our preclinical murine model. In the present study, we established a unique murine model that presents aggressive features concerning cell growth and infiltration in SCID mice within 3 weeks. Thus, it represents a novel model to evaluate tissue toxicity and the efficacy of therapeutic agents directed toward the treatment of EBV-associated lymphoproliferative diseases.

The blood-plasma ritonavir concentrations obtained in the therapy of HIV-infection are between 5 to 15 I M,[34] but much higher maximal concentrations (up to 46 I M) have been demonstrated in individual patients.[35] In the present study, we used the concentration of ritonavir for doing *in vitro* experiments from 0 to 40 I M and *in vivo* 30 mg/kg/day used for treatment of AIDS patients. Constitutive and strong NF-jB activation was reported to be a characteristic of LCL and important for LCL growth and survival.[7] Our results indicate that inhibition of NF-jB activity by ritonavir reduced cell growth and induced apoptosis of these cells. This is consistent with down-modulation of NF-jB regulated genes such as antiapoptotic and cell-cycle related genes. Our murine model clearly indicate that 30 mg/kg/day of ritonavir (the same dose used clinically for treating HIV/AIDS patients) significantly inhibits EBV-transformed cell growth and infiltration into various organs of NOG mice. The plasma exposure produced by this dose in mice is only approximately one-half of the plasma exposure observed with the licensed dose of ritonavir in human (600 mg BID). In our murine model, ritonavir at this treatment dosage is well tolerated without severe adverse effects observed in the mice during the treatment period. These data strongly suggest that the HIV protease inhibitor, ritonavir, is a promising antitumor agent against EBV-transformed cells and could be used clinically for treatment of EBV-associated malignancies. These results suggest that anti-tumor activity of ritonavir correlates with suppression of NF-jB activity.

In summary, we have established a novel NOG EBV-associated lymphoma model that presents features similar to patients with EBV-infection in immunocompromised patients. These results also indicate that the HIV protease inhibitor, ritonavir, showed antitumor and anti-NF-jB activity against EBV-transformed cells. Finally, our results strongly suggest that NF-jB serves as a potential molecular target to treat EBV-associated malignancies, and that ritonavir might be used clinically as a single compound or in combination with the reducing dose of chemotherapeutic agents for treatment of patients with life-threatening EBV-associated lymphoproliferative diseases and AIDS-associated lymphomas.

Acknowledgements

We thank D. Kempf and T. Yamada of Abbott Laboratories, S. Ichinose of Instrumental Analysis Research Center and S. Endo of Animal Research Center, Tokyo Medical and Dental University for their advice and assistance with the experiments. We also thank Y. Sato of the National Institute of Infectious Diseases for her excellent technical assistance.

References

1. Rickinson AB, Kieff E. Epstein-Barr virus. In: Fields BN, ed. Fields virology, 4th edn. New York (NY): Lippincott Williams and Wilkins, 2001. Vol. 1, 2575–627.
2. Kieff E, Rickinson AB. Epstein-Barr virus and replication. In: Fields BN, ed. Fields virology, 4th ed. New York (NY): Lippincott Williams and Wilkins, 2001. Vol. 1, 2511–73.
3. Zur Hausen H, Schulte-Holthausen H. Presence of EB virus nucleic acid homology in a "virus-free" line of Burkitt tumour cells. Nature 1970;227:245–48.
4. Nonoyama M, Pagano JS. Homology between Epstein-Barr virus DNA and viral DNA from Burkitt's lymphoma and nasopharyngeal carcinoma determined by DNA-DNA reassociation kinetics. Nature 1973;242:44–7.
5. Rowe M, Lear AL, Croom-Carter D, Davies AH, Rickinson AB. Three pathways of Epstein-Barr virus gene activation from EBNA1-positive latency in B lymphocytes. J Virol 1992;66:122–31.
6. Yamamoto N, Takizawa T, Iwanaga Y, Shimizu N, Yamamoto N. Malignant transformation of B lymphoma cell line BJAB by Epstein-Barr virus-encoded small RNAs. FEBS Lett 2000;484:153–58.
7. Mosialos G, Birkenbach M, Yalamanchili R, VanArsdale T, Ware C, Kieff E. The Epstein-Barr virus transforming protein LMP1 engages signaling proteins for the tumor necrosis factor receptor family. Cell 1995;80:389–99.
8. Mori N, Fujii M, Ikeda S, Yamada Y, Tomonaga M, Ballard DW, Yamamoto N. Constitutive activation of NF-jB in primary adult T-cell leukemia cells. Blood 1999;93:2360–8.
9. Baldwin AS. The NF-jB and IjB proteins: new discoveries and insights. Annu Rev Immunol 1999;14:649–81.
10. Guinness ME, Kenney JL, Reiss M, Lacy J. Bcl-2 antisense oligodeoxynucleotide therapy of Epstein-Barr virus-associated lymphoproliferative disease in severe combined immunodeficient mice. Cancer Res 2000;60:5354–8.
11. Miyake A, Dewan MZ, Ishida T, Watanabe M, Honda M, Sata T, Yamamoto N, Umezawa K, Watanabe T, Horie R. Induction of apoptosis in Epstein-Barr virus-infected B-lymphocytes by the NF-kappaB inhibitor DHMEQ. Microbes Infect 2008;10:748–56.
12. Watanabe M, Dewan MZ, Okamura T, Sasaki M, Itoh K, Higashihara M, Mizoguchi H, Honda M, Sata T, Watanabe T, Yamamoto N, Umezawa K, et al. A novel NF-jB inhibitor DHMEQ selectively targets constitutive NF-jB activity and induces apoptosis of multiple myeloma cells in vitro and in vivo. Int J Cancer 2005;114:32–8.
13. Adams J, Palombella VJ, Elliott PJ. Proteasome inhibition: a new strategy in cancer treatment. Invest New Drugs 2001;18:109–21.
14. Teicher BA, Ara G, Herbst R, Palombella VJ, Adams J. The proteasome inhibitor PS-341 in cancer therapy. Clin Cancer Res 1999; 5:2638–45.

15. Hideshima T, Chauhan D, Richardson P, Mitsiades C, Mitsiades N, Hayashi T, Munshi N, Dang L, Castro A, Palombella V, Adams J, Anderson KC. NF-j B as a therapeutic target in multiple myeloma. J Biol Chem 2002;277:16639–47.
16. Dewan MZ, Terashima K, Taruishi M, Hasegawa H, Ito M, Tanaka Y, Mori N, Sata T, Koyanagi Y, Maeda M, Kubuki Y, Okayama A, et al. Rapid tumor formation of human T-cell leukemia virus type 1-infected cell lines in novel NOD-SCID/gc^{null} mice: suppression by an inhibitor against NF-j B. J Virol 2003;77:5286–94.
17. Kitajima I, Shinohara T, Bilakovics J, Brown DA, Xu X, Nerenberg M. Ablation of transplanted HTLV-I Tax-transformed tumors in mice by antisense inhibition of NF-j B. Science 1992;258:1792–5.
18. Mori N, Yamada Y, Ikeda S, Yamasaki Y, Tsukasaki K, Tanaka Y, Tomonaga M, Yamamoto N, Fujii M. Bay 11–7082 inhibits transcription factor NF-j B and induces apoptosis of HTLV-I-infected T-cell lines and primary adult T-cell leukemia cells. Blood 2002;100:1828–34.
19. Tan C, Waldmann TA. Proteasome inhibitor PS-341, a potential therapeutic agent for adult T-cell leukemia. Cancer Res 2002;62: 1083–6.
20. Dewan MZ, Uchihara JN, Terashima K, Honda M, Sata T, Ito M, Fujii N, Uozumi K, Tsukasaki K, Tomonaga M, Kubuki Y, Okayama A, et al. Efficient intervention of growth and infiltration of primary adult T-cell leukemia cells by an HIV protease inhibitor, ritonavir. Blood 2006;107:716–24.
21. Cahir-McFarland ED, Davidso DM, Schauer SL, Duong J, Kieff E. NF-kappa B inhibition causes spontaneous apoptosis in Epstein-Barr virus-transformed lymphoblastoid cells. Proc Natl Acad Sci USA 2000;97:6055–60.
22. Collier AC. Efficacy of combination antiretroviral therapy. Adv Exp Med Biol 1996;394:355–72.
23. Collier AC, Coombs RW, Schoenfeld DA, Bassett R, Baruch A, Corey L. Combination therapy with zidovudine, didanosine and saquinavir. Antiviral Res 1996;29:99.
24. Collier AC, Coombs RW, Schoenfeld DA, Bassett RL, Timpone J, Baruch A, Jones M, Facey K, Whitacre C, McAuliffe VJ, Friedman HM, Merigan TC, et al. Treatment of human immunodeficiency virus infection with saquinavir, zidovudine, and zalcitabine. AIDS Clinical Trials Group. N Engl J Med 1996;334:1011–17.
25. Markowitz M, Saag M, Powderly WG, Hurley AM, Hsu A, Valdes JM, Henry D, Sattler F, La Marca A, Leonard JM, Ho DD. A preliminary study of ritonavir, an inhibitor of HIV-1 protease, to treat HIV-1 infection. N Engl J Med 1995;333:1534–39.
26. Kempf DJ, Marsh KC, Denissen JF, McDonald E, Vasavanonda S, Flentge CA, Green BE, Fino L, Park CH, Kong XP, Wideburg NE, Saldivar A, et al. ABT-538 is a potent inhibitor of human immunodeficiency virus protease and has high oral bioavailability in humans. Proc Natl Acad Sci USA 1995;92:2484–88.
27. Andre P, Groettrup M, Klenerman P, de Giuli R, Booth BL, Jr, Cerundolo V, Bonneville M, Jotereau F, Zinkernagel RM, Lotteau V. An inhibitor of HIV-1 protease modulates proteasome activity, antigen presentation, and T cell responses. Proc Natl Acad Sci USA 1998; 95:13120–24.
28. Liang JS, Distler O, Cooper DA, Jamil H, Deckelbaum RJ, Ginsberg HN, Sturley SL. HIV protease inhibitors protect apolipoprotein B from degradation by the proteasome: a potential mechanism for protease inhibitor-induced hyperlipidemia. Nat Med 2001;7:1327–31.
29. Schmidtke G, Holzhütter HG, Bogyo M, Kairies N, Groll M, de Giuli R, Emch S, Groettrup M. How an inhibitor of the HIV-I protease modulates proteasome activity. J Biol Chem 1999;274:35734–40.
30. Gaedicke S, Firat-Geier E, Constantiniu O, Lucchiari-Hartz M, Freudenberg M, Galanos C, Niedermann G. Antitumor effect of the human immunodeficiency virus protease inhibitor ritonavir: induction of tumor-cell apoptosis associated with perturbation of proteasomal proteolysis. Cancer Res 2002;62:6901–8.
31. Pati S, Pelser CB, Dufraine J, Bryant JL, Reitz JMS, Weichold FF. Antitumorigenic effects of HIV protease inhibitor ritonavir: inhibition of Kaposi sarcoma. Blood 2002;99:3771–9.
32. Sgadari C, Barillari G, Toschi E, Carlei D, Bacigalupo I, Baccarini S, Palladino C, Leone P, Bugarini R, Malavasi L, Cafaro A, Falchi M, et al. HIV protease inhibitors are potent anti-angiogenic molecules and promote regression of Kaposi sarcoma. Nat Med 2002;8:225–32.
33. Katano H, Pesnicak H, Cohen JI. Simvastatin induces apoptosis of Epstein-Barr virus (EBV)-transformed lymphoblastoid cell lines and delays development of EBV lymphomas. Proc Natl Acad Sci USA 2004;101:4960–5.
34. Norvir, Ritonavir Product monograph. North Chicago, IL: Abbott laboratories, 1997.
35. Gatti G, Di Biagio A, Casazza R, De Pascalis C, Bassetti M, Cruciani M, Vella S, Bassetti D. The relationship between ritonavir plasma levels and side-effects: implications for therapeutic drug monitoring. AIDS 1999;13:2083–9.

JOURNAL OF VIROLOGY, Dec. 2008, p. 11958–11963
0022-538X/08/$08.00+0 doi:10.1128/JVI.01149-08

Vol. 82, No. 23

NOTES

Critical Role for TSLC1 Expression in the Growth and Organ Infiltration of Adult T-Cell Leukemia Cells In Vivo▽

M. Zahidunnabi Dewan,[1,2]† Naofumi Takamatsu,[3] Tomonori Hidaka,[4] Kinta Hatakeyama,[5] Shingo Nakahata,[3] Jun-ichi Fujisawa,[6] Harutaka Katano,[7] Naoki Yamamoto,[1,2]* and Kazuhiro Morishita[3]*

Department of Molecular Virology, Graduate School, Tokyo Medical and Dental University, 1-5-45 Yushima, Bunkyo-ku, Tokyo 113-8519, Japan[1]; AIDS Research Center, National Institute of Infectious Disease, 1-23-1 Toyama, Shinjuku-ku, Tokyo 162-8640, Japan[2]; Department of Medical Sciences,[3] Department of Internal Medicine,[4] and Department of Pathology,[5] Faculty of Medicine, University of Miyazaki, Kiyotake, Miyazaki, Japan; Department of Microbiology, Kansai Medical University, Moriguchi, Osaka, Japan[6]; and Department of Pathology, National Institute of Infectious Diseases, 1-23-1 Toyama, Shinjuku-ku, Tokyo 162-8640, Japan[7]

Received 2 June 2008/Accepted 15 September 2008

Adult T-cell leukemia (ATL) is associated with human T-cell leukemia virus type 1 infection. The tumor suppressor lung cancer 1 (TSLC1) gene was previously identified as a novel cell surface marker for ATL, and this study demonstrated the involvement of TSLC1 expression in tumor growth and organ infiltration of ATL cells. In experiments using NOD/SCID/γc^{null} mice, both leukemia cell lines and primary ATL cells with high TSLC1 expression caused more tumor formation and aggressive infiltration of various organs of mice. Our results suggest that TSLC1 expression in ATL cells plays an important role in the growth and organ infiltration of ATL cells.

Human T-cell leukemia virus type 1 (HTLV-1) is the causative agent of an aggressive form of $CD4^+$ T-cell leukemia termed adult T-cell leukemia (ATL) (7, 14, 18). Carriers of HTLV-1 have been identified in a number of locations throughout the world, including parts of Africa; Papua New Guinea; specific regions in Europe including Romania; parts of South America including northern Brazil, Peru, northern Argentina, and Colombia; and the southern part of Kyushu in Japan (17). Common findings in patients with ATL include enlargement of peripheral lymph nodes, hepatomegaly, splenomegaly, skin infiltration, and hypercalcemia. The Tax gene is a unique viral gene thought to play a central role in HTLV-1-induced transformation. It is responsible for transactivation of the HTLV-1 long terminal repeat (5, 16) and numerous cellular genes involved in T-cell activation and growth, including those encoding interleukin-2 (IL-2) (11) and the α chain of IL-2 receptor (IL-2Rα) (CD25, Tac) (1, 2). The long latency of ATL development suggests that multiple genetic events accumulate in HTLV-1-infected cells; however, the precise molecular mechanisms of ATL leukemogenesis following HTLV-1 infection have not been fully elucidated.

The tumor suppressor lung cancer 1 gene (TSLC1) at chromosome 11q23 has been identified as a tumor suppressor gene in non-small-cell lung cancer (9, 13). In contrast, it was recently found to be highly and ectopically expressed in acute-type ATL cells, most ATL cell lines, and HTLV-1-infected T-cell lines (15). Enforced expression of TSLC1 in ATL-derived ED-40515(−) cells resulted in higher aggregations and binding abilities in a human umbilical vein endothelial cell line (HUVEC). These results suggest that TSLC1 might contribute to tumor growth by enhancing aggregation after infiltration and migration outside blood vessels. Since the role of TSLC1 overexpression in the course of tumor growth and organ infiltration of ATL cells remains to be fully elucidated, we investigated the direct involvement of TSLC1 in the growth and infiltration of leukemia cells using C57BL/6J and NOD-SCID/γc^{null} (NOG) mice (4, 8).

In order to analyze the tumorigenicity of TSLC1 expression in leukemia cells, a murine IL-2-independent T-lymphoma cell line (EL4) injected into the intraperitoneum of syngeneic C57BL/6J mice was used as a model for ATL. EL4 cells were transfected with a pcDNA3 expression plasmid containing TSLC1, and transformant cells were selected by a limiting-dilution method in the presence of G-418. We also used EL4 cells expressing a green fluorescent protein-Tax fusion protein (EL4/GAX) (6) and parental EL4 (EL4/p) as a control. Expression of Tax protein in EL4 cells, a 38-kDa band of Tax protein in HUT102 cells, and a 64-kDa band of green fluorescent protein-Tax fusion protein in EL4/GAX cells were all

* Corresponding author. Mailing address for Naoki Yamamoto: AIDS Research Center, National Institute of Infectious Disease, 1-23-1 Toyama, Shinjuku-ku, Tokyo 162-8640, Japan. Phone: 81-3-5285-1111. Fax: 81-3-5285-1165. E-mail: nyama@nih.go.jp. Mailing address for Kazuhiro Morishita: Division of Tumor and Cellular Biochemistry, Department of Medical Sciences, Faculty of Medicine, University of Miyazaki, Kiyotake, Miyazaki, Japan. Phone: 81-9-8585-0985. Fax: 81-9-8585-2401. E-mail: kmorishi@med.miyazaki-u.ac.jp.

† Present address: Department of Pathology, New York University School of Medicine, 550 First Avenue, New York, NY 10016.

▽ Published ahead of print on 15 October 2008.